biology

MDPI

Article

RNA*i* and Metabolomic Profiling Reveal CHH-Mediated Hepatopancreatic Metabolic Regulation During Ovarian Development in *Scylla paramamosain*

Wen-Feng Li [1,2,3,*], Guang-Yu Jiang [1,3], Yi-Fei Wang [1,3], Jing Sun [1,3], Jie Liu [1,3], An-Qi Zhao [1,3], Yan Chen [1,2,3], Zhao-Yang Yin [4], Shan Zhang [1], Shou-Yang Zhou [3], Xiang-Yi Xu [3], Yue-Cheng Zhong [3] and Hai Huang [1,2,3,*]

1 Yazhou Bay Innovation Institute, Hainan Tropical Ocean University, Sanya 572022, China
2 Key Laboratory of Utilization and Conservation for Tropical Marine Bioresources (Hainan Tropical Ocean University), Ministry of Education; Hainan Key Laboratory for Conservation and Utilization of Tropical Marine Fishery Resources, Hainan Tropical Ocean University, Sanya 572022, China
3 College of Fisheries and Life Science, Hainan Tropical Ocean University, Sanya 572022, China
4 Hainan Key Laboratory of Tropical Aquatic Germplasm, Sanya Oceanographic Institution, Ocean University of China, Sanya 572024, China
* Correspondence: liwenfeng2369@163.com (W.-F.L.); huanghai74@126.com (H.H.)

Simple Summary

The mud crab *Scylla paramamosain* is recognized as an economically important crustacean species widely cultured along the tropical and subtropical coastlines of China. Mature females with fully developed ovaries command high commercial value, yet the endocrine mechanisms underlying ovarian maturation remain poorly understood. Crustacean hyperglycemic hormone (CHH) is a well-documented neuroendocrine factor involved in the regulation of energy metabolism and reproductive processes in decapod crustaceans. In this study, CHH transcript expression was knocked down via double-stranded RNA-mediated interference and histological assessments with untargeted metabolomic profiling were applied to investigate its regulatory roles. Our findings indicate that CHH suppression attenuates hepatopancreatic metabolic and secretory activity, induces targeted reprogramming of major nutrient metabolic pathways, and slows ovarian developmental progression. Ovarian tissue nevertheless retains gradual developmental growth likely via compensatory metabolic adjustments. These results expand current knowledge of crustacean reproductive physiology and offer candidate metabolic targets for controlled gonadal development in commercial crab aquaculture.

Abstract

Crustacean hyperglycemic hormone (CHH) is a key neuroendocrine factor involved in the regulation of energy metabolism and reproductive development in crustacean species. The mechanisms by which CHH mediates hepatopancreatic metabolic reprogramming during ovarian development remain poorly understood. In this study, *Scylla paramamosain* was used as the experimental model. CHH transcript expression in eyestalk ganglia was knocked down via double-stranded RNA (dsRNA)-mediated RNA interference. The regulatory effects of CHH gene silencing on physiological phenotypes, hepatopancreatic structure, and metabolic profiles were systematically evaluated via histological assessments and untargeted metabolomics profiling. The results sindicated that CHH dsRNA injection induced substantial knockdown of CHH transcription, with sustained silencing efficacy throughout the experimental period. In the long-term RNA*i* trial, the hepatosomatic index (HSI) exhibited a modest increase in the CHH dsRNA

Academic Editor: Yafei Duan

Received: 22 October 2026
Revised: 23 November 2026
Accepted: 25 November 2026
Published: 26 November 2026

Copyright: © 2026 by the authors. Licensee MDPI, Basel, Switzerland. This article is an open access article distributed under the terms and conditions of the Creative Commons Attribution (CC BY) license.

treatment group (DSI), while the gonadosomatic index (GSI) was significantly lower than that in the saline control group (SAI). Histological observations suggested that *CHH* silencing moderately reduced hepatopancreatic metabolic and secretory activity. Metabolomic profiling identified 146 significantly different metabolites, including 47 with elevated abundance and 99 with reduced abundance. These metabolites were primarily categorized into four major chemical classes: amino acids and their derivatives, lipids, carbohydrates, and steroids. Metabolite set enrichment analysis (MSEA) revealed 12 significantly enriched pathways. Positively enriched pathways mainly concentrated in nucleotide metabolism and multiple amino acid metabolic pathways. In contrast, negatively enriched pathways were dominated by carbohydrate and lipid metabolism, including glycerophospholipid metabolism, starch and sucrose metabolism, and nucleotide sugar biosynthesis. KEGG pathway enrichment analysis indicated that fructose and mannose metabolism, together with amino sugar and nucleotide sugar metabolism, represented core pathways underlying the metabolic phenotypic differences between the two groups. Global topological analysis of the metabolic network further identified six core differential pathway modules, which collectively formed a coordinated regulatory network covering carbon metabolism, amino acid biosynthesis, and nucleotide metabolism. Collectively, suppression of *CHH* expression may attenuate nutrient transport and metabolic capacity of hepatopancreas, trigger metabolic reprogramming by modulating core pathways involved in carbohydrate, amino acid, and nucleotide metabolism, and may ultimately delay ovarian development. These results provide experimental insights into the metabolic regulatory mechanisms underlying reproductive development in crustaceans, and may inform the identification of metabolic targets for the precise regulation of gonadal development in aquaculture practices.

Keywords: *Scylla paramamosain*; crustacean hyperglycemic hormone (CHH); RNA interference; hepatopancreas; ovarian development

1. Introduction

The mud crab *Scylla paramamosain* is a commercially important portunid species distributed along the tropical and subtropical coasts of China. The species is well recognized for its rapid growth, delicate meat texture, and high nutritional value. Mature females with fully developed ovaries, commonly marketed as red-roe crabs, are particularly prized and remain in persistent short supply [1]. According to the 2026 China Fishery Statistical Yearbook, total annual production of mud crabs (*Scylla* spp.) from wild capture and marine aquaculture reaches approximately 230,000 metric tons. Furthermore, most current farming operations rely heavily on wild-caught juvenile crabs for stocking, a practice that exerts mounting pressure on wild populations and coincides with gradual declines in both farming area and capture yield in recent years [1,2] .

Ovarian maturation represents a core biological process that underpins reproductive performance in crustaceans. In mud crabs, this process is highly complex and encompasses vitellogenesis, endocrine secretion, and nutrient deposition [3,4]. Morphologically, the H-shaped ovary of *S. paramamosain* consists of symmetrical lobes joined by a central bridge, situated dorsally to the stomach and hepatopancreas in the cephalothorax and extending posteriorly along either side of the hindgut [5]. Ovarian development is initiated following mating that occurs during the reproductive molt, when spermatophore transfer triggers rapid ovarian growth; unmated females typically show delayed or arrested ovarian development [6,7]. Ovarian maturation is commonly

classified into five stages based on the gonadosomatic index (GSI) and morphological criteria: Stage I (pre-developmental), characterized by translucent, thin, and smooth ovaries; Stage II (initial developmental/pre-vitellogenesis), with enlarged, creamy-white ovarian tissue; Stage III (proliferative/primary vitellogenesis), featuring further expanded, pale-yellow ovaries with distinct lobulation; Stage IV (pre-maturation/secondary vitellogenesis), with markedly enlarged, bright-yellow ovaries bearing well-developed lobules; and Stage V (maturation/tertiary vitellogenesis), in which ovaries occupy most available space in the body cavity, range from bright orange to reddish in color, and display fully swollen lobules [5,8–10].

The full ovarian cycle in *Scylla* spp. lasts approximately 55 to 60 days, modulated by a range of environmental and endogenous factors, including hormonal regulation, salinity, natural diet, tissue biochemical composition, and digestive enzyme activity [11]. Preliminary data from laboratory rearing trials in our laboratory indicate that the period from reproductive molt to initial developmental/pre-vitellogenesis averages 5 to 7 days. In comparison, the transition from early to proliferative/primary vitellogenesis remains relatively stable at 14 to 16 days. The duration from primary vitellogenesis through pre-maturation to full maturation shows greater inter-individual variation, averaging 20 to 40 days. The relatively stable duration of the early-to-primary vitellogenesis interval renders this period a suitable developmental window for investigating the regulatory mechanisms governing nutrient and energy metabolism during ovarian development.

The hepatopancreas is the primary organ for nutrient absorption, storage, metabolism, and mobilization in crustaceans, and it plays a critical role in supporting lipid and nutrient accumulation during ovarian maturation [4,12]. Across ovarian developmental stages, the levels of proteins, lipids, and other nutrients undergo substantial alterations in both the hepatopancreas and ovary, indicating active translocation, metabolic transformation, and deposition of major nutrients between these two tissues. Vitellin (Vn), a high-density glycolipophosphoprotein bearing carbohydrate, phosphate, and lipid moieties, is produced via proteolytic cleavage of vitellogenin (VTG) and constitutes the major yolk protein in crustacean oocytes [11,13]. In mud crabs, vitellogenesis occurs in both the hepatopancreas and ovary: VTG is synthesized and processed into Vn subunits in the hepatopancreas, then released into the hemolymph and taken up by growing oocytes [14]. The hepatopancreas acts as the major extraovarian synthetic organ for vitellogenin, supplying most yolk precursor substances during ovarian development, especially in the initial vitellogenic stage (stage I). Ovarian vitellogenin synthesis contributes only a minor supplement, and its functional role tends to be more pronounced in later vitellogenic stages [15]. In this context, characterization of hepatopancreatic metabolic profiles of carbohydrates, lipids, and amino acids throughout ovarian development may elucidate nutrient transport, metabolism, and deposition, as well as the underlying molecular regulatory mechanisms.

Crustacean hyperglycemic hormone (CHH) is a pivotal neuropeptide regulator in crustacean physiology. Initially identified as a mediator of stress-induced hyperglycemia by modulating carbohydrate metabolism, CHH has since been established as a pleiotropic hormone involved in lipid metabolism, reproductive regulation, osmoregulation, immune responses, molting, and metamorphosis [16–19]. Despite its pleiotropic functions, the primary and best-characterized action of CHH remains the regulation of carbohydrate metabolism, mainly by modulating the activity and expression of key glycogen-metabolizing enzymes to mobilize tissue glycogen reserves [20]. In *S. paramamosain*, CHH transcript levels in the eyestalk ganglia increase progressively from stage I to stage IV of ovarian development and decrease at the mature stage, suggesting a potential stimulatory role, direct or indirect, in vitellogenic processes [21].

Nevertheless, the specific functions and underlying mechanisms of CHH in ovarian development remain largely undefined.

RNA interference (RNA*i*) mediated by sequence-specific double-stranded RNA (dsRNA) serves as a robust tool for functional genomic studies in crustaceans [11,20–23]. Building on previous findings, this study focused on the transition from early to primary vitellogenesis, a period of consistent developmental progression, and combined dsRNA-mediated CHH silencing with hepatopancreatic metabolomic profiling. This study aimed to investigate the regulatory role of CHH in hepatopancreatic energy and nutrient metabolism during ovarian development and to provide a theoretical basis for regulating ovarian maturation in cultured mud crab broodstock.

2. Materials and Methods

2.1. Experimental Animals

All animal experimental protocols were reviewed and approved by the Laboratory Animal Management and Ethics Committee of Hainan Tropical Ocean University (KJCLL-2026-026). Experimental animals were selected and maintained following a previously established protocol [24]. In brief, all *S. paramamosain* individuals used in this study originated from pond aquaculture systems in Wanning, Hainan Province, China. Prior to the screening of experimental animals, the crabs had been reared in farm ponds for approximately three months. All crabs selected for the experiment were virgin females with no prior reproductive history. Subadult females before mating generally weigh between 100 and 150 g, and we further narrowed the selection range to 120 ± 10 g for improved experimental uniformity. Before indoor acclimation, the molt stage of female crabs was determined according to morphological changes in the swimming legs, as previously described [24,25]. Only healthy individuals approaching the pre-molt stage, with intact appendages and rapid escape responses to external stimuli such as manual disturbance, were retained for the experiment. A total of 300 *S. paramamosain* individuals (150 females and 150 males; female body weight: 120 ± 10 g, male body weight: 150 ± 10 g) were purchased and reared under laboratory conditions. Healthy females at the pre-molt stage were selected and reared individually with one male crab. Each mating pair was maintained in an independent glass tank (80 cm × 60 cm × 40 cm) at 27 ± 1 °C and fed with clam meat twice daily; water salinity was maintained at 18 ± 2 ‰. Additional rearing parameters were maintained as follows: a 12 h light: 12 h dark photoperiod was maintained throughout the experimental period. Water temperature, 28–32 °C; pH, 7.4–8.0; dissolved oxygen ≥ 6.0 mg/L; ammonia nitrogen ≤ 0.20 mg/L; nitrite ≤ 0.1 mg/L. Regular partial water exchange was performed to preserve water quality stability. The crabs were fed at a daily ration of 8–10% of their body weight, with two separate feedings delivered in the morning and evening. All tanks were inspected four times daily to monitor the occurrence of pubertal molt. The laboratory acclimation period varied from one to three weeks, until the crabs completed their pubertal molt and mated with males thereafter. Immediately following the completion of pubertal molt and mating, male crabs were removed from the rearing units, and female individuals were maintained separately for subsequent trials [24,25]. After pubertal molt, female crabs were maintained for 7 days before experimental use.

2.2. Production of CHH Double-Stranded RNAs (dsRNAs)

A partial fragment of the CHH gene was amplified via polymerase chain reaction (PCR) using the primer pair as follows: dsRNA-*CHH*3-F (5′-TTCGATAAAATGACAACTCTGGCAG-3′) and dsRNA-*CHH*3-R (5′-AGATTTCCACGTTCTTGCCCAAATC-3′) [23]. PCR amplification was carried out in a

50 µL reaction mixture containing 1× PCR buffer, 200 µM dNTPs, 0.2 µM each primer, 1.25 U high-fidelity DNA polymerase (Takara Bio, Shiga, Japan), and template cDNA. The thermal cycling conditions were as follows: initial denaturation at 94 °C for 3 min; 35 cycles of denaturation at 94 °C for 30 s, annealing at 58 °C for 30 s, and extension at 72 °C for 30 s; and a final extension at 72 °C for 10 min [23]. The target PCR amplicon was separated via 1% agarose gel electrophoresis, then recovered and purified using a gel extraction kit.

The purified PCR fragment was ligated into the linearized pGEM-T Easy Vector (Promega, Madison, WI, USA), which carries T7 and SP6 bacteriophage promoters flanking the multiple cloning site. The ligation product was transformed into competent *Escherichia coli* DH5α cells. Positive recombinant clones were screened via blue-white screening and confirmed by colony PCR and Sanger sequencing. Confirmed recombinant plasmids were extracted with a plasmid purification kit. To prepare templates for in vitro transcription, the recombinant pGEM-T Easy-*CHH*3 plasmid was linearized via digestion with a single restriction enzyme that does not cleave within the CHH3 insert. For sense strand transcription, the plasmid was digested at the restriction site downstream of the insert on the SP6 promoter side, allowing transcription to terminate at the linearized end. For antisense strand transcription, the plasmid was digested at the restriction site flanking the 5′ end of the insert on the distal T7 promoter side, enabling SP6 RNA polymerase to transcribe the full insert. Complete linearization was verified via 1% agarose gel electrophoresis. The linearized DNA was purified and eluted in RNase-free water. In vitro transcription was performed separately for each strand. Sense single-stranded RNA (ssRNA) was transcribed from the T7 promoter using T7 RNA polymerase, and antisense ssRNA was synthesized from the SP6 promoter using SP6 RNA polymerase. Following transcription, RNase-free DNase I was added to each reaction, and the mixture was incubated at 37 °C for 30 min to digest the linearized DNA template, followed by heat inactivation at 65 °C for 10 min. The resulting sense and antisense ssRNA products were purified separately.

Equimolar quantities of purified sense and antisense ssRNA were mixed in annealing buffer. The mixture was denatured at 95 °C for 5 min and then gradually cooled to room temperature at a rate of 0.1 °C/s to facilitate strand annealing and dsRNA formation. Residual unannealed ssRNA was removed via mild RNase treatment. The dsRNA was purified and quantified using a NanoDrop spectrophotometer, and its integrity was evaluated via 1.5% agarose gel electrophoresis. Aliquots of dsRNA were stored at −80 °C prior to injection. *Green fluorescent protein (GFP)* dsRNA was synthesized in parallel as a negative control following the same protocol.

2.3. CHH Gene Silencing Efficiency Assay

Female crabs at 7 days post-pubertal molt received intramuscular injection into the arthrodial membrane of the fifth pereiopod using a syringe fitted with a 29-gauge needle. Four experimental groups were established for this assay: an untreated group without any injection procedure (without any treatment, 0 h), a saline injection group (SAI) treated with crab physiological saline, a *CHH* dsRNA injection group (DSI) treated with *CHH* double-stranded RNA, and a *GFP* dsRNA group (GFP) treated with green fluorescent protein double-stranded RNA. Crabs in the SAI, DSI, and GFP groups received 100 µL of crab saline (pH 7.4), 100 µL CHH dsRNA-saline suspension, and 100 µL of GFP dsRNA-saline suspension, respectively, at a dosage of 5 µg dsRNA per gram body weight. Each treatment included three biological replicates (n = 3). Eyestalk ganglia and hemolymph samples were collected from individual samples in the untreated (0 h) group as baseline. For the SAI, DSI and GFP dsRNA groups, eyestalk ganglia and

hemolymph samples (GFP group: eyestalk ganglia only) were collected at 24, 48, 72, 96 and 120 h post-injection (hpi) to evaluate CHH gene silencing efficiency, respectively. Briefly, total RNA was extracted from eyestalk ganglia using the Purescript RNA Isolation Kit (Gentra Systems, Minneapolis, MN, USA), and then treated with RQ1 RNase-free DNase (Promega, Madison, WI, USA) following the manufacturer's instructions. Reverse transcription was performed for cDNA synthesis as previously described [20,26]. The resulting cDNA was stored at −20 °C until subsequent quantitative real-time PCR (qPCR) analysis. Hemolymph glucose analysis for individuals in the untreated, SAI and DSI groups were performed using a Glucose (GO) Assay Kit (Sigma-Aldrich, St. Louis, MO, USA) following the manufacturer's instruction, respectively [23]. Each sample was analyzed with at least three replicates (n = 3).

2.4. Long-Term RNA Interference Experiment

Based on these validation results, a long-term CHH gene-silencing experiment was conducted in female *S. paramamosain* during ovarian development. Crabs at stage II of ovarian maturation were used for the experiment [5,8–10]. Briefly, CHH dsRNA was diluted in crustacean saline to the concentration and volume validated in the preceding assays. Female crabs sampled at the start of the experiment served as the baseline group (sampled at day 0; Figure S1A) for ovarian developmental staging, hepatosomatic index (HSI), and gonadosomatic index (GSI) determination. The dsRNA solution was injected into crabs in the treatment group (DSI; day 15, Figure S1C), while an equal volume of crab saline was administered to the control group (SAI; day 15, Figure S1B). Booster injections were administered on days 6 and 11 after the initial injection. The experiment lasted 15 days, and each crab received three injections. Each treatment included six biological replicates (n = 6). Hepatopancreatic tissue samples were collected from individuals in SAI and DSI groups for histological sectioning and H&E staining (n = 3), and metabolomic analysis (n = 6) at 15 days post-injection. Long-term CHH gene silencing efficiency was assessed via quantitative real-time PCR (qPCR) on eyestalk ganglion tissues collected from individual samples collected at 0, 3, 6, 9, 12, and 15 days post-injection, with three independent biological replicates per group (n = 3).

At the end of the experiment, crabs were surface-sterilized and dissected on ice. Intact hepatopancreas and ovarian tissues were dissected and weighed to calculate HSI and GSI, respectively. Ovarian morphology and coloration, together with HSI and GSI values, were used to determine the ovarian developmental stage of sampled female *S. paramamosain*. Aliquots of both tissues were fixed in 4% paraformaldehyde and processed for hematoxylin and eosin (H&E) staining. The remaining tissue samples were snap-frozen in liquid nitrogen and stored at −80 °C. Hepatopancreas specimens were reserved for subsequent metabolomic profiling.

2.5. Quantitative Real-Time Polymerase Chain Reaction (qPCR)

qPCR was employed to evaluate the effects of CHH and GFP dsRNA on the expression of the target CHH gene. qPCR was run on a CFX384 Touch Real-Time PCR System (Bio-Rad, Hercules, CA, USA) using FastStart Universal SYBR Green Master Mix (Roche Diagnostics, Indianapolis, IN, USA). The primer pairs were as follows: the forward sequence (CHH-F): CTTCTCTACGAGGCTCCTAATGC, the reverse sequence (CHH-R): CTAAATAGTTGTGCTGCGATACG [23]. The cycling conditions were as follows: initial denaturation at 95 °C for 10 min; 40 cycles of denaturation at 95 °C for 15 s, annealing at 60 °C for 60 s, and extension at 72 °C for 30 s; and a final extension at 72 °C for 10 min. The ramp rate was set to 20 °C/s. Elongation factor 1α (EF1α; GenBank accession no. JQ824130.1) was used as the reference gene for relative quantification of target gene ex-

pression. The $2^{-\Delta\Delta Ct}$ method was adopted to calculate relative gene expression levels across all samples [26].

2.6. UHPLC-MS/MS Metabolite Analysis

Approximately 25 mg of each tissue sample (n = 6) was weighed and mixed with 500 μL of pre-chilled extraction solvent kept at −40 °C. The extraction solvent was a methanol: acetonitrile: water mixture (2:2:1, *v*/*v*/*v*) spiked with internal standards. The mixture was homogenized at 35 Hz for 4 min and then sonicated in an ice-water bath for 5 min. The combined homogenization and sonication procedure was repeated three times in total. The mixture was then incubated at −40 °C for 1 h for static extraction. After filtration, a 300 μL aliquot of supernatant was collected, and the filtrate was transferred for instrumental analysis. Chromatographic separation was performed on a Vanquish UHPLC system (Thermo Fisher Scientific, Waltham, MA, USA) equipped with a Waters ACQUITY UPLC BEH Amide column (2.1 mm × 50 mm, 1.7 μm; Waters Corp., Milford, MA, USA). Mobile phase A was an aqueous solution containing 25 mmol/L ammonium acetate and 25 mmol/L ammonia, and mobile phase B was acetonitrile. The gradient elution was performed at a constant flow rate of 0.50 mL/min: 0.00–0.25 min, 95% B; 0.25–3.50 min, 95–65% B; 3.50–4.00 min, 65–40% B; 4.00–4.50 min, 40% B; 4.50–4.55 min, 40–95% B; 4.55–6.00 min, 95% B. The autosampler chamber was maintained at 4 °C, and each sample was injected at 2 μL.

For sample quality control, a pooled quality control sample was prepared by mixing equal volumes from all experimental samples. Three quality control samples were distributed across the 12-sample analytical batch to monitor the stability of the analytical system throughout data acquisition. An isotope-labeled internal standard was spiked into all samples. The internal standard was maintained at a uniform concentration across all quality control samples, providing an additional benchmark for assessing analytical consistency.

A standardized data processing workflow was applied to raw spectral data prior to statistical analysis, which comprised four core steps. First, outlier filtering was performed on individual features to remove background noise, with outliers identified and excluded based on the relative standard deviation, also referred to as the coefficient of variation. Second, missing value filtering was conducted at the feature level. Peak area data were retained only when missing values accounted for no more than 50% within a single group, or no more than 50% across all experimental groups. Third, missing value imputation was implemented for the filtered dataset. Missing entries were replaced with a value equivalent to half of the minimum detected intensity for each corresponding feature. Fourth, data normalization was performed using the total ion current of each individual sample.

Primary (level 1) and secondary (level 2) mass spectrometry data were acquired using an Orbitrap Exploris 120 mass spectrometer (Thermo Fisher Scientific, Waltham, MA, USA) controlled by Xcalibur software (version 4.4, Thermo Fisher Scientific, Waltham, MA, USA). Metabolite identifications were annotated in accordance with the confidence classification framework defined by the Metabolomics Standards Initiative (MSI). Level 1 designation applies to metabolites that show concordant MS1 spectra, MS2 fragmentation patterns and retention time with authentic reference standards analyzed under identical experimental conditions. Level 2 designation refers to metabolites whose MS1 and MS2 spectral profiles match entries deposited in public spectral databases. Key instrumental parameters were set as follows: sheath gas flow rate, 50 Arb; auxiliary gas flow rate, 15 Arb; capillary temperature, 320 °C; full scan mass resolution, 60,000; MS/MS resolution, 15,000; and stepped normalized collision energy, 20/30/40 eV.

The spray voltage was set to 3.8 kV for positive ionization mode and −3.4 kV for negative ionization mode. Raw mass spectrometry files were converted to mzXML format using ProteoWizard software (version 3.0.24054). Metabolite annotation was conducted using an in-house R package developed by our research consortium, with metabolite matching performed against the BiotreeDB database (version 3.0, BIOTREE Biological Technology Co., Ltd., Shanghai, China). A separate custom R package developed in our laboratory was used for subsequent data visualization.

2.7. Statistical and Multivariate Analysis of Metabolites

The Shapiro–Wilk test was used to evaluate normality, while Levene's test was applied to check variance homogeneity. Independent two-sample t-test were performed for parametric data, and the Mann–Whitney U test was used for non-parametric data at a significance level of 0.05. For high-dimensional metabolomic datasets, raw *p*-values derived from t-tests or Mann–Whitney U tests were further adjusted by the Benjamini–Hochberg procedure to control the false discovery rate (FDR). Statistical analyses were performed in R (v4.2.1) using the packages car (Levene's test), rstatix (t-test, Mann–Whitney U), and stats (shapiro.test, p.adjust, method = BH). Principal component analysis (PCA) and orthogonal partial least squares discriminant analysis (OPLS-DA) were performed with in-house R scripts for automated model construction. Prior to PCA, data were subjected to logarithmic transformation followed by mean centering. Prior to OPLS-DA modeling, logarithmic transformation combined with unit variance scaling was applied for data pretreatment. A permutation test with 200 random iterations was conducted to generate reference OPLS-DA models, from which R^2 and Q^2 values of the permuted models were derived. Candidate differential metabolites and volcano plots were generated based on two filtering criteria: (1) statistical significance (FDR-adjusted $p < 0.05$) and (2) variable importance in projection (VIP) score > 1.

Metabolite set enrichment analysis (MSEA), KEGG enrichment analysis, and pathway analysis were performed based on pathway-associated metabolite sets. For topology analysis, the pathway library was set to *S. paramamosain* KEGG pathways, with global test algorithm and relative betweenness centrality selected as the enrichment method and topological metric, respectively.

3. Results

3.1. qPCR-Based Assessment of CHH Gene Silencing Efficiency

Quantitative real-time PCR (qPCR) analysis showed that *CHH* double-stranded RNA (dsRNA; DSI group) induced significantly suppression of *CHH* transcription in eyestalk ganglia at 24, 48, 72, 96, and 120 h post-injection (hpi). Relative to the saline-injected control group (SAI group), *CHH* transcript levels in the DSI group declined to 38.11%, 41.10%, 49.23%, 43.15%, and 65.86% of the control levels at the five corresponding time points, respectively (Figure 1). *CHH* transcript levels exhibited a very gradual recovery over the observation period, with the gene silencing effect sustained over an extended timeframe. At 5 days after dsRNA administration, *CHH* expression in the DSI group remained below 70% of the control level, indicating sustained and appreciable gene silencing efficacy. No significant differences in *CHH* transcript abundance were found between the GFP dsRNA injection group (GFP) and the saline-injected group (SAI) across the five days following injection (Figure S2).

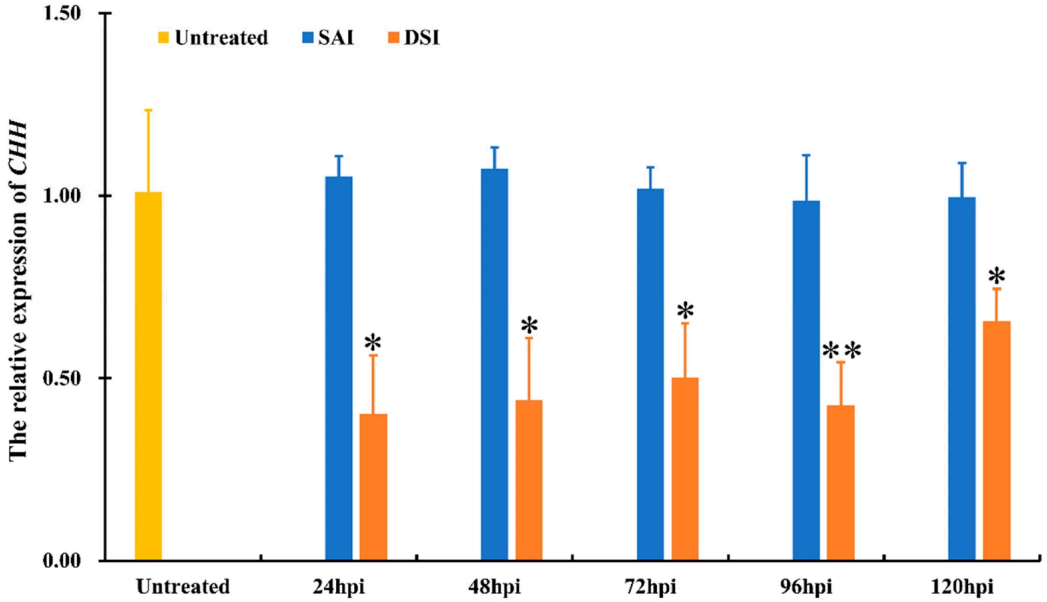


Figure 1. The relative CHH gene expression in eyestalk ganglia post injection. DSI, *CHH* dsRNA injection group; SAI, crab saline injection group. *, $p < 0.05$; **, $p < 0.01$.

3.2. Glucose Level in Hemolymph After CHH dsRNA Injection

Measurements of hemolymph glucose revealed that glucose concentrations tended to decrease significantly following CHH gene silencing within the initial 72 h relative to the saline control group (Figure 2). A gradual recovery of glucose levels could be observed over longer incubation periods, and no statistically significant differences were detected after 72 h (Figure 2).

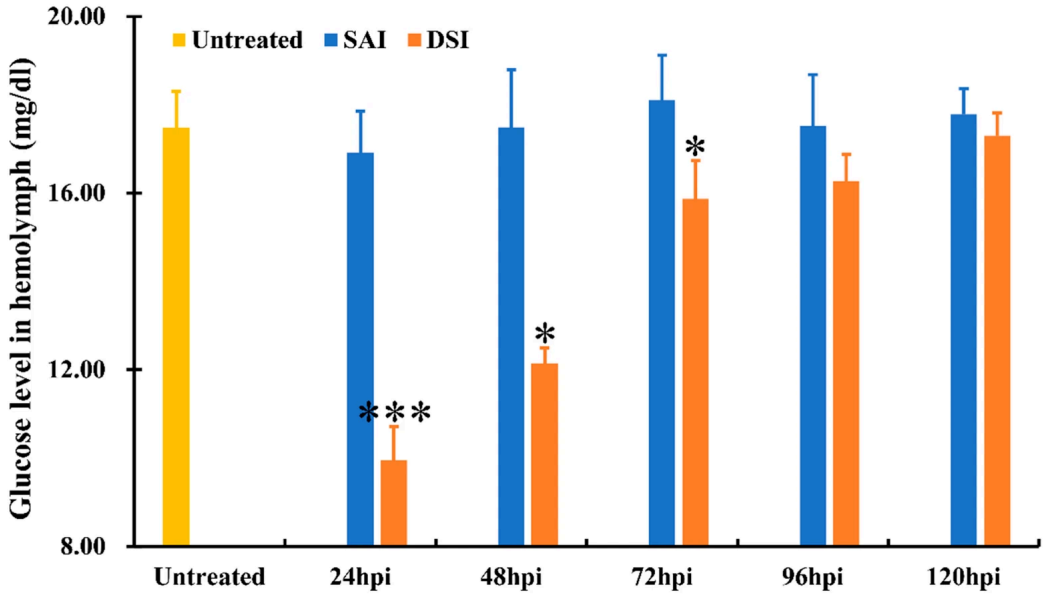


Figure 2. Glucose level in hemolymph of *S. paramamosain*. Untreated group, without any injection; DSI, *CHH* dsRNA injection group; SAI, crab saline injection group. *, $p < 0.05$, ***, $p < 0.001$.

3.3. qPCR-Based Assessment of CHH Gene Silencing Efficiency in Long-Term Trials

qPCR assays were carried out to monitor changes in *CHH* transcript abundance within eyestalk ganglia at 0, 3, 6, 9, 12, and 15 days during a 15-day trial of sustained *CHH* transcript suppression. Relative to the saline-injected group (SAI), the *CHH* dsRNA

treatment group (DSI) exhibited estimated silencing efficiencies of 41.72%, 42.75%, 40.96%, 41.15%, and 46.44% on 3, 6, 9, 12, and 15 days post-injection, respectively. Measurable declines in *CHH* transcript levels were detected at these sampling time points. The collected data may support the view that *CHH* dsRNA could mediate persistent downregulation of target transcripts in eyestalk ganglia over the experimental period. The observed reduction, nevertheless, appears to represent partial transcript suppression and does not correspond to complete transcriptional ablation (Figure 3).

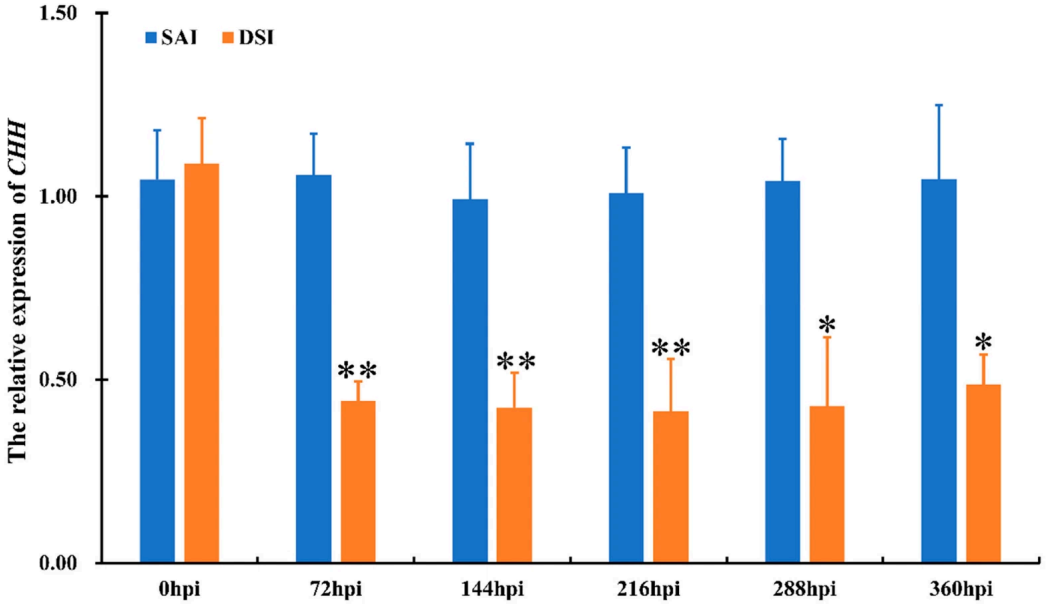


Figure 3. The relative CHH gene expression post *CHH* dsRNA injection in long-term *CHH* silencing trial. DSI, *CHH* dsRNA injection group; SAI, crab saline injection group. *, $p < 0.05$, **, $p < 0.01$.

3.4. Comparison and Histological Characteristics of the Hepatopancreas

Body weight (BW), gonadosomatic index (GSI), and hepatosomatic index (HSI) were determined over the course of the long-term crustacean hyperglycemic hormone (CHH) gene silencing trial, with samples collected at trial initiation serving as the baseline control group (day 0; Table S1). The saline-injected group (SAI) exhibited the greatest BW gain, followed by the CHH dsRNA-injected group (DSI). Both treatment groups showed greater BW gain than the Control group; however, no statistically significant differences were detected in pairwise comparisons showed statistically significant differences in BW among the three groups. For HSI, the DSI group showed the largest increase, followed by the SAI group and the Control group, with no significant intergroup differences. This trend suggests that CHH gene silencing may partially weaken the capacity for mobilizing amino acids, lipids and carbohydrates from the hepatopancreas to other tissues. Greater nutrient retention within this organ could occur under such conditions, which may contribute to a modest upward trend in the hepatosomatic index observed in the DSI group. Residual CHH transcripts may still support the regulation of substance transport and metabolic processes within hepatopancreatic tissues, given the incomplete suppression of target gene expression. Such residual activity might allow continued morphological development of the hepatopancreas in dsRNA-treated individuals.

GSI displayed a distinct pattern compared with BW and HSI. GSI values ranked in descending order as follows: SAI > DSI > baseline group. The DSI group showed a significantly lower GSI than the SAI group, whereas both treatment groups had significantly higher GSI values than the baseline group (Table S1). These observations indicate that al-

though CHH gene silencing may impair nutrient and energy substrate transport to the ovary and possibly slow ovarian development, the ovary continues to grow throughout the experimental period. It is likely that alternative metabolic fluxes support sustained ovarian development under *CHH* suppression, or the residual CHH could additionally sustain ovarian development via direct or indirect mechanisms.

At stage II of ovarian development (Figure 4), hepatopancreatic tubules exhibited normal morphology, with a characteristic star-shaped central lumen (L). The basement membrane (BM) was continuous and clearly delineated, with epithelial cells arranged compactly. The two principal functional cell types, blister cells (B) and resorptive cells (R), showed normal morphology. Interstitial tissue and hemolymph sinuses were uniformly distributed among tubules, with no histological abnormalities detected (Figure 4 A). In the SAI group (Figure 4B), hepatopancreatic tubule diameter increased alongside luminal dilation, consistent with the progression of ovarian development. Epithelial cell height increased, and resorptive cells contained more cytoplasmic vacuoles. These morphological changes may reflect enhanced absorptive and metabolic capacity to meet the nutritional demands of gonadal development. Blister cell density also increased moderately, consistent with relatively elevated secretory activity. The basement membrane remained intact, with no signs of structural disruption. In the DSI group (Figure 4C), the overall structural architecture of hepatopancreatic tubules was maintained during ovarian development, with an intact basement membrane and no organic lesions, such as epithelial necrosis or desquamation. Compared with the stage-matched SAI group, tubule diameters were remarkably reduced (Figure 4D), and luminal dilation was less pronounced. These morphological features may indicate a significant reduction in hepatopancreatic metabolic and secretory activity.

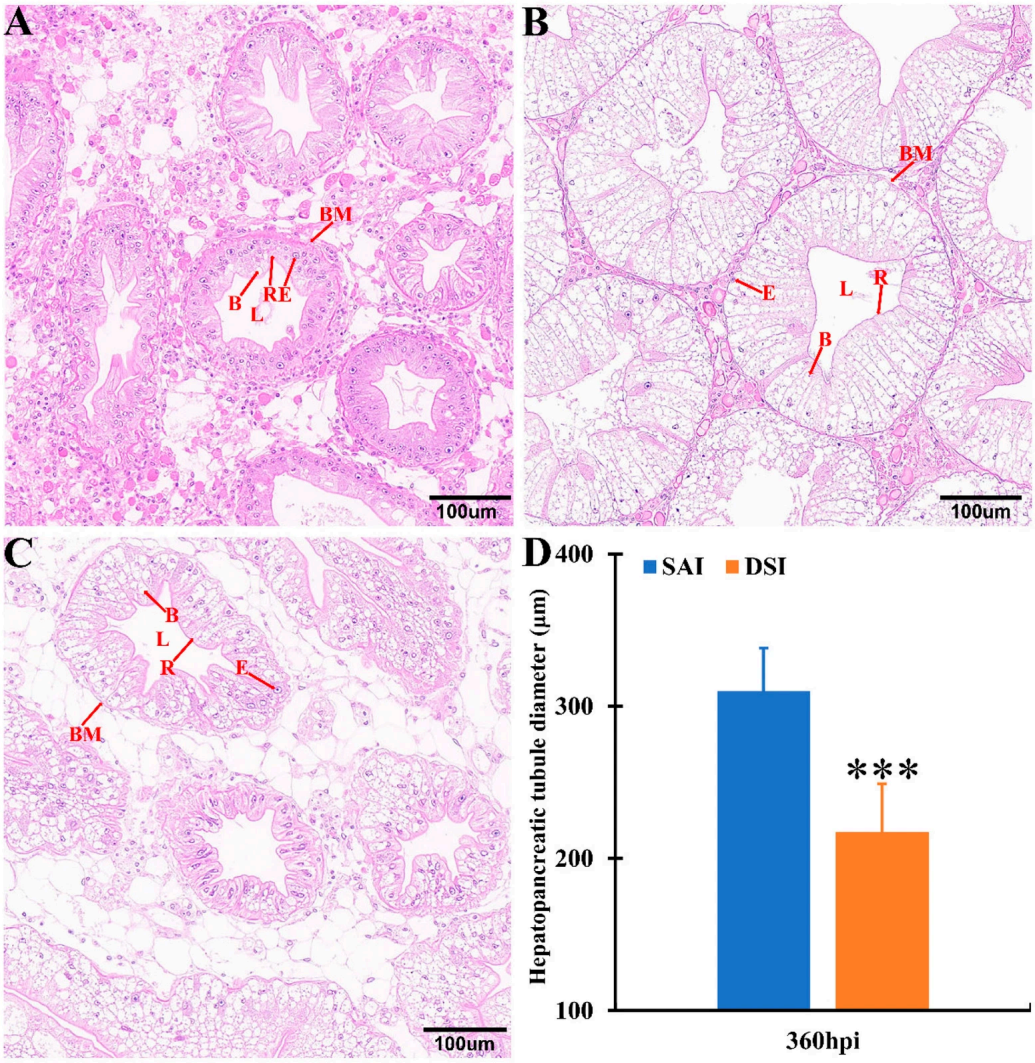


Figure 4. Hepatopancreatic sections with H&E staining at the initiation of the long-term RNAi trial ((**A**) 0 days post injection) and at the trial termination in the crab saline group ((**B**) SAI, 15 days post injection) and CHH dsRNA treatment group ((**C**) DSI, 15 days post injection), and the outer diameter of hepatopancreatic tubules in the SAI and DSI groups (**D**). BM, basement membrane; R, R cell; B, B cell; E, E cell; L, lumen. DSI, *CHH* dsRNA injection group; SAI, crab saline injection group. ***, $p < 0.001$.

3.5. Metabolite Identification and Classification Annotation

A total of 3105 metabolites were identified in the present study and categorized into a hierarchical system based on chemical structure and metabolic function. As illustrated in the two-tiered circular diagram, we assigned all metabolites to 7 superclasses, which we further divided into 37 classes (Figure 5A). Figure 5B shows the relative abundance of each metabolite category at the superclass level. Amino acids and their derivatives represented the most abundant chemical category, accounting for the largest proportion of the annotated metabolome. Lipids were the second most abundant superclass. The remaining superclasses, ranked by descending abundance, included phenylpropanoids, carbohydrates, others, organic acids and derivatives, and terpenoids and steroid derivatives. Collectively, amino acids and lipids accounted for most of the metabolome profile, while the remaining categories contributed to a diverse metabolic background.

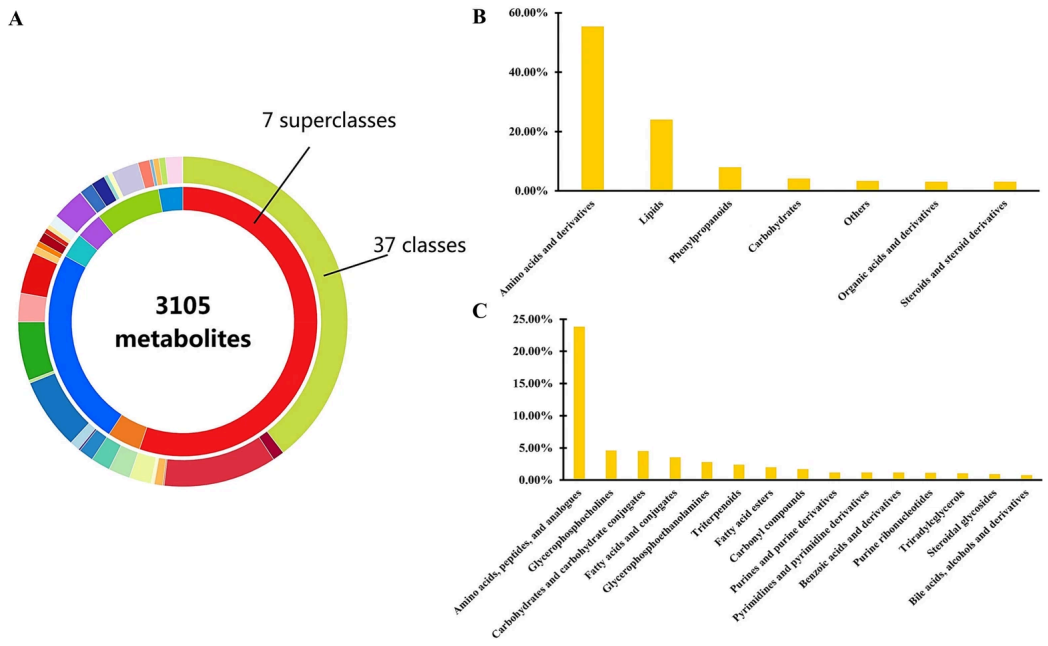


Figure 5. Number of metabolites classified at the superclass and class levels (**A**), the categories and relative proportions of metabolites at the superclass (**B**) and class (**C**) levels.

Figure 5C shows the relative proportions of the top 15 metabolite classes. Amino acids, peptides, and analogs accounted for the highest proportion, representing a key subclass of the amino acids and derivatives superclass. Other predominant subclasses included glycerophosphocholines, carbohydrates and carbohydrate conjugates, fatty acids and conjugates, and glycerophosphoethanolamines, which fell under the lipid and carbohydrate superclasses, respectively. The proportions of remaining subclasses, such as triterpenoids, fatty acid esters, carbonyl compounds, purine and pyrimidine derivatives, and bile acids and derivatives, decreased sequentially.

3.6. Principal Component Analyses

Unsupervised principal component analysis (PCA) was performed to assess overall metabolic variation across samples. The first principal component (PC1) explained 29.9% of the total variance, and the second principal component (PC2) explained 19.7%, with a cumulative explained variance of 49.6%. Although the proportion of explained variance was moderate, the SAI group (red circles) and DSI group (blue squares) showed a relatively clear separation trend within the 95% confidence ellipses. Samples from each group clustered closely in the multivariate projection, with no severe outliers, suggesting differences in overall metabolic profiles between the two groups and good experimental reproducibility (Figure 6A).

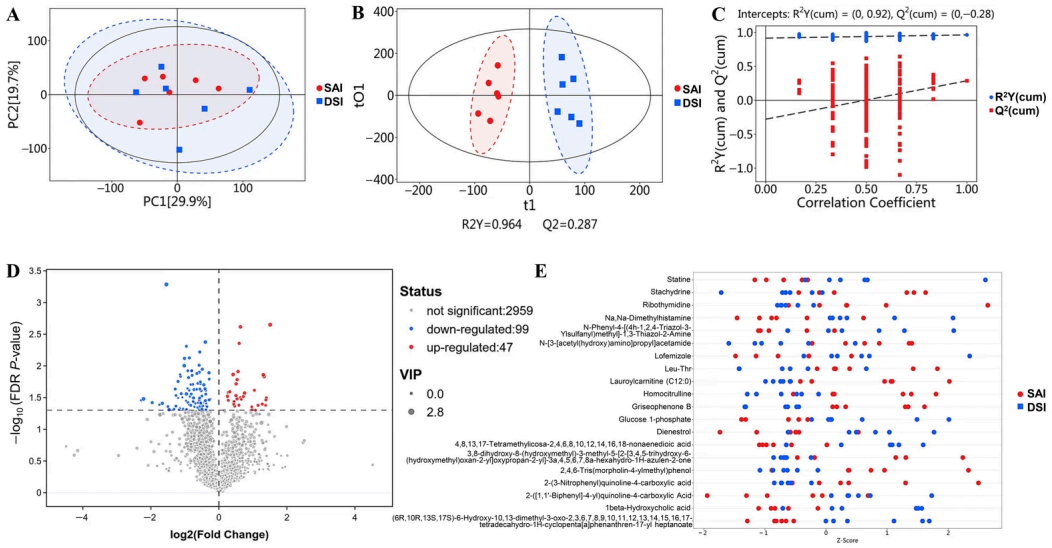


Figure 6. Multivariate analysis of hepatopancreatic metabolites between the crab saline group (SAI) and CHH dsRNA treatment group (DSI). (**A**) PCA score plot; (**B**) OPLS-DA score plot; (**C**) Permutation test; (**D**) Volcano plot of differential metabolites; (**E**) Z-score plot.

Orthogonal partial least squares discriminant analysis (OPLS-DA) showed complete separation between the SAI and DSI groups along the t1 principal component: samples fell on opposite sides of the 95% confidence ellipse, with no overlap, indicating significant differences in their metabolic profiles. The model yielded an R^2Y of 0.964, indicating relatively high explanatory power for intragroup metabolic variation, and a Q2 value of 0.287, in comparison, suggesting that the model exhibits only moderate limited external predictive performance (Figure 6B).

A permutation test using 200 random permutations was conducted to validate the OPLS-DA model. As the retention proportion (correlation coefficient) increased from 0 to 1, the cumulative R^2Y and Q^2 values of the permuted models gradually decreased. All permuted models had lower Q^2 (cum) values than the original model. The vertical intercepts were −0.28 for Q^2 (cum) and 0.92 for R^2Y (cum). These results met the validity criteria for permutation tests, indicating that the established OPLS-DA model was not overfitted and supporting its reliability for subsequent differential metabolite screening (Figure 6C).

3.7. Differential Metabolite Analysis

A volcano plot was generated to identify significantly differential metabolites after CHH RNA interference (FDR p value < 0.05 and VIP > 1); compared with the SAI group, we identified 146 significantly differential metabolites in the DSI group, including 47 metabolites with elevated abundance and 99 metabolites with reduced abundance. The remaining 2959 metabolites showed no statistically significant differences between groups (Figure 6D).

Z-score normalization revealed distinct concentration distributions and change trends of differential metabolites between the two groups. For instance, metabolites such as stachydrine and ribothymidine showed significantly higher levels in the DSI group relative to the SAI group, whereas 1β-hydroxycholic acid and 2-(1,1′-biphenyl-4-yl) quinoline-4-carboxylic acid showed higher Z-scores in the SAI group. These patterns matched the up- and down-regulation trends in the volcano plot, further confirming differential metabolite abundance between groups (Figure 6E).

3.8. Metabolite Sets Enrichment Analysis (MSEA)

Metabolite sets enrichment analysis (MSEA) was performed as follows: all metabolites were ranked by the magnitude of their differential expression between the two sample groups, and statistical tests were conducted to determine whether predefined metabolite sets were enriched at the top or bottom of the ranked list [21,22]. In this study, MSEA was performed based on metabolic pathway gene sets of *S. paramamosain*. NES (Normalized Enrichment Score) represents the enrichment trend of metabolites in the ranked list; positive NES indicates that metabolites of the pathway tend to be highly abundant in the DSI group, while negative NES indicates the opposite. A total of 12 metabolic pathways were found to be significantly enriched, including 6 pathways with positive enrichment trends (normalized enrichment score, NES > 0) and 6 pathways with negative enrichment trends (NES < 0; Table 1).

Table 1. MSEA for the metabolic profiles in hepatopancreas.

ID	Description	NES	*p*-Value	Leading_Edge
sprm00564	Glycerophospholipid metabolism—*Scylla paramamosain* (green mud crab)	−1.90277	0.00511	tags = 56%, list = 26%, signal = 43%
sprm01250	Biosynthesis of nucleotide sugars—*Scylla paramamosain* (green mud crab)	−1.87797	0.00575	tags = 82%, list = 17%, signal = 70%
sprm00500	Starch and sucrose metabolism—*Scylla paramamosain* (green mud crab)	−1.82221	0.00835	tags = 57%, list = 7%, signal = 54%
sprm00400	Phenylalanine, tyrosine and tryptophan biosynthesis—*Scylla paramamosain* (green mud crab)	−1.74357	0.01015	tags = 33%, list = 10%, signal = 30%
sprm00541	Biosynthesis of various nucleotide sugars—*Scylla paramamosain* (green mud	−1.76472	0.01828	tags = 80%, list = 17%, signal = 68%

ID	Description	NES	*p*-Value	Leading_Edge
	crab)			
sprm00520	Amino sugar and nucleotide sugar metabolism—*Scylla paramamosain* (green mud crab)	−1.65602	0.03526	tags = 78%, list = 17%, signal = 66%
sprm00240	Pyrimidine metabolism—*Scylla paramamosain* (green mud crab)	1.62811	0.01596	tags = 50%, list = 22%, signal = 40%
sprm01232	Nucleotide metabolism—*Scylla paramamosain* (green mud crab)	1.57873	0.02039	tags = 50%, list = 22%, signal = 41%
sprm00260	Glycine, serine and threonine metabolism—*Scylla paramamosain* (green mud crab)	1.57297	0.02223	tags = 55%, list = 35%, signal = 37%
sprm00220	Arginine biosynthesis—*Scylla paramamosain* (green mud crab)	1.52086	0.03760	tags = 50%, list = 12%, signal = 45%
sprm00410	beta-Alanine metabolism—*Scylla paramamosain* (green mud crab)	1.50130	0.04406	tags = 56%, list = 16%, signal = 47%
sprm00230	Purine metabolism—*Scylla paramamosain* (green mud crab)	1.48511	0.04146	tags = 46%, list = 20%, signal = 38%

Specifically, negatively enriched pathways indicated remarkable metabolic down-regulation in the DSI group across three major functional categories: carbohydrate me-

tabolism, lipid metabolism, and amino acid biosynthesis. Among these, glycerophospholipid metabolism (sprm00564) showed the highest enrichment level (NES = −1.903, p = 0.0051). Leading edge analysis indicated that 56% of metabolites in this pathway were in the core enriched subset (tags), with the top 26% of pathway members contributing most of the enrichment signal (list), corresponding to a core signal strength of 43%. Biosynthesis of nucleotide sugars (sprm01250) and starch and sucrose metabolism (sprm00500) ranked second in enrichment. In addition, phenylalanine, tyrosine, and tryptophan biosynthesis (sprm00400), biosynthesis of various nucleotide sugars (sprm00541), and amino sugar and nucleotide sugar metabolism (sprm00520) all showed significant negative enrichment, further supporting the overall attenuation of carbohydrate metabolism and aromatic amino acid synthesis pathways.

In contrast, positively enriched pathways indicated an overall elevation in metabolic activity in the DSI group, primarily affecting nucleotide and amino acid metabolism. Pyrimidine metabolism (sprm00240) showed the strongest downregulation (NES = 1.628, p = 0.0160), followed by nucleotide metabolism (sprm01232), which included 25 metabolites and was the largest gene set in this analysis. Other negatively enriched pathways included glycine, serine, and threonine metabolism (sprm00260); arginine biosynthesis (sprm00220); beta-alanine metabolism (sprm00410); and purine metabolism (sprm00230). Together, these pathways span key nodes in amino acid synthesis and purine/pyrimidine nucleotide metabolism (Table 1).

Collectively, the MSEA results indicated clear pathway clustering in metabolic differences between the DSI and SAI groups. Downregulated pathways were dominated by substance production and energy metabolism, including glycerophospholipid metabolism, starch and sucrose metabolism, and nucleotide sugar metabolism, whereas upregulated pathways mainly involved nucleotide metabolism and multiple amino acid metabolism pathways. Together, these pathways constituted the core metabolic regulatory network underlying the phenotypic differences between groups.

3.9. KEGG Enrichment Analysis

To systematically characterize the regulatory features of pathways mediated by differential metabolites, we performed a differential abundance enrichment analysis using the KEGG metabolic pathway database. Pathways were quantified by p-value and differential abundance score (DA Score) to reflect overall changes in pathway activity. The differential abundance score (DA score) reflects the overall directional change in all metabolites in a pathway; positive values indicate overall upregulation of the pathway, and negative values indicate overall downregulation. A total of 15 significantly enriched metabolic pathways were screened, including 5 downregulated and 10 upregulated pathways.

The 5 significantly downregulated pathways were mainly clustered into three categories: carbohydrate metabolism, glycan biosynthesis and metabolism, and global and overview pathways. Ranked by decreasing enrichment significance, these included fructose and mannose metabolism (sprm00051) and amino sugar and nucleotide sugar metabolism (sprm00520), both belonging to carbohydrate metabolism; biosynthesis of various nucleotide sugars (sprm00541), belonging to glycan biosynthesis and metabolism; and biosynthesis of nucleotide sugars (sprm01250) and biosynthesis of cofactors (sprm01240), belonging to global and overview pathways. These results suggest that overall activity in carbohydrate metabolism and sugar nucleotide synthesis-related pathways was significantly inhibited, representing a core downregulated feature of metabolic differences between groups (Table 2).

Table 2. KEGG enrichment analysis for the metabolic profiles in hepatopancreas.

	Pathway	Description	Class	*p*_Value	DA_Score
Down	sprm01250	Biosynthesis of nucleotide sugars	Global and overview maps	0.00482	−0.33333
	sprm01240	Biosynthesis of cofactors	Global and overview maps	0.01859	−0.17647
	sprm00051	Fructose and mannose metabolism	Carbohydrate metabolism	0.00011	−0.75000
	sprm00520	Amino sugar and nucleotide sugar metabolism	Carbohydrate metabolism	0.00025	−0.42857
	sprm00541	Biosynthesis of various nucleotide sugars	Glycan biosynthesis and metabolism	0.00111	−0.37500
Up	sprm01100	Metabolic pathways	Global and overview maps	0.03363	0.07273
	sprm01232	Nucleotide metabolism	Global and overview maps	0.00001	0.20000
	sprm00240	Pyrimidine metabolism	Nucleotide metabolism	0.00002	0.26667
	sprm01230	Biosynthesis of amino acids	Global and overview maps	0.00461	0.12500
	sprm00230	Purine metabolism	Nucleotide metabolism	0.00235	0.18750
	sprm00220	Arginine biosynthesis	Amino acid metabolism	0.00003	0.50000
	sprm00250	Alanine, aspartate and glutamate metabolism	Amino acid metabolism	0.00258	0.25000
	sprm00410	beta-Alanine metabolism	Metabolism of other amino acids	0.00336	0.25000
	sprm00470	D-Amino acid metabolism	Metabolism of other amino acids	0.01542	0.11111
	sprm00190	Oxidative phosphorylation	Energy metabolism	0.03292	0.50000

In contrast, the 10 significantly upregulated pathways spanned multiple functional categories, including nucleotide metabolism, amino acid metabolism, energy metabolism, and global and overview pathways, indicating widespread metabolic activation. These included nucleotide metabolism (sprm01232, global and overview pathway), pyrimidine metabolism (sprm00240, nucleotide metabolism category), arginine biosynthesis (sprm00220, amino acid metabolism category), purine metabolism (sprm00230, nucleotide metabolism category), alanine, aspartate, and glutamate metabolism (sprm00250, amino acid metabolism category), beta-alanine metabolism (sprm00410, other amino acids category), biosynthesis of amino acids (sprm01230, global and overview pathway), D-amino acid metabolism (sprm00470, other amino acids category), oxidative phosphorylation (sprm00190, energy metabolism category), and metabolic pathways (sprm01100, global and overview pathway). Among these, arginine biosynthesis (sprm00220) was one of the most upregulated pathways, with a change magnitude comparable to oxidative phosphorylation (sprm00190) (Table 2).

From a functional-category perspective, nucleotide metabolism (including the pyrimidine and purine branches) and amino acid metabolism (including arginine synthesis, alanine metabolism, and other branches) were the core functional modules with the strongest upregulation. Oxidative phosphorylation, an energy metabolism pathway, was also substantially upregulated. Together, these changes suggest that metabolic remodeling between groups centered on nucleic acid synthesis and amino acid metabolism, alongside an overall increase in energy metabolism.

3.10. Metabolic Pathway Analysis

Analysis of key regulatory pathways mediated by differential metabolites, based on the KEGG metabolic pathway database, yielded the following findings. Fructose and mannose metabolism showed the highest enrichment significance, indicating the strongest statistical evidence across all pathways. Amino sugar and nucleotide sugar metabolism ranked second in significance. In addition, nitrogen metabolism and pyrimidine metabolism both reached significance. Overall, carbohydrate metabolism-related pathways accounted for most of the highly significant pathways, representing the core enriched functional category of metabolic differences between groups (Figure 7).

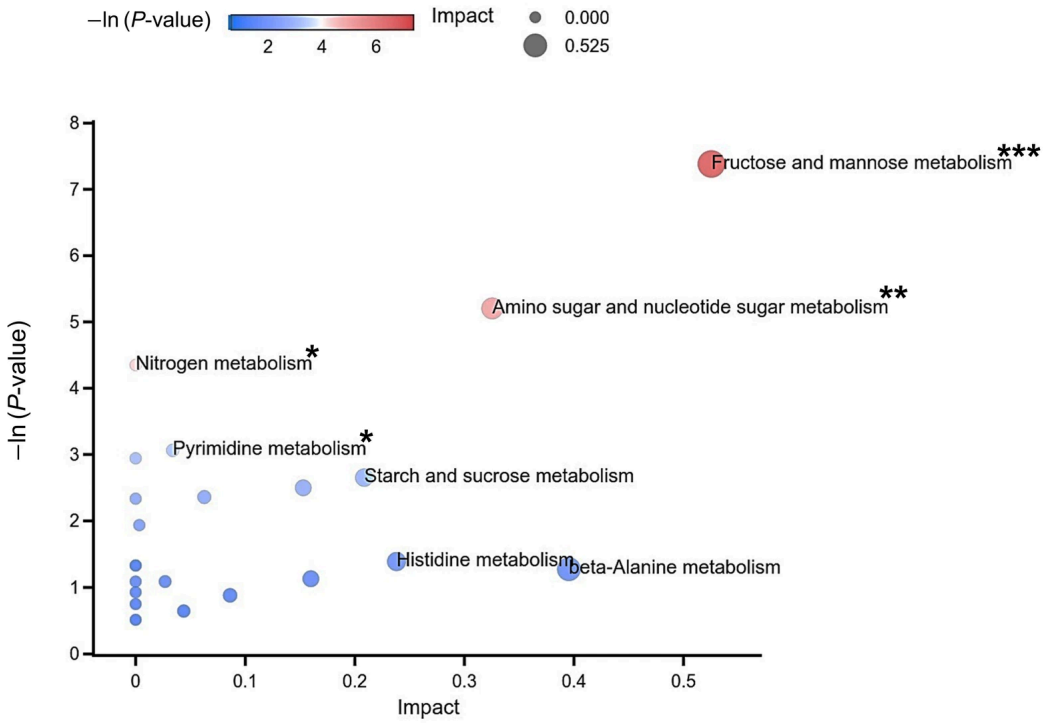


Figure 7. Significantly altered metabolic pathways. *, $p < 0.05$; **, $p < 0.01$; ***, $p < 0.001$.

Pathway impact values, derived from metabolic network topology, reflect the centrality of differential metabolites and the overall regulatory influence within each pathway. From a topological perspective, fructose and mannose metabolism and amino sugar and nucleotide sugar metabolism had higher impact values and the greatest enrichment significance, identifying them as core pathways regulating metabolic phenotypic differences between groups. Beta-alanine metabolism, histidine metabolism, and starch and sucrose metabolism had moderate pathway impacts but relatively low enrichment significance. By contrast, nitrogen and pyrimidine metabolism showed significant enrichment but near-zero impact values, suggesting that their differential metabolites mainly occupied peripheral nodes with limited topological regulatory effects on the pathway as a whole.

Combined analyses of statistical significance and topological impact identified fructose and mannose metabolism, along with amino sugar and nucleotide sugar metabolism, as the study's most critical differential metabolic pathways. Both pathways were highly statistically significant and functionally important within the network, acting as core regulatory nodes that mediate metabolic phenotypic differences between the two groups.

3.11. The Significantly Changed Metabolites

A total of 146 hepatopancreatic metabolites were significantly altered in the DSI group compared with the SAI group. These differential metabolites belonged to four major chemical categories: amino acids and derivatives (84 metabolites), lipids (29 metabolites), carbohydrates (14 metabolites), and steroids and steroid derivatives (4 metabolites, Table S1).

Within the amino acid and derivative category, 27 metabolites were significantly more abundant in the DSI group. These upregulated metabolites were mainly methylated amino acids, indole carboxylic acid derivatives from the tryptophan pathway, functional heterocyclic molecules, and pyrimidine-related derivatives. The other 57 metabolites in this category were significantly less abundant, including 35 amino acid deriva-

tives, 16 dipeptides, 5 free amino acids, and 1 tripeptide. Notably, the free amino acids glutamine, beta-alanine, histidine, homocitrulline, and theanine all showed significant reductions in the DSI group (Table S1). Of the 29 differentially abundant lipids, 7 were significantly upregulated in the DSI group, primarily medium- and short-chain acylcarnitines, glycerophospholipids, and selected terpenoid derivatives. The remaining 22 were significantly downregulated: 6 fatty acids and conjugates, 5 prenol lipids, 4 polyketides, 2 carnitines, 2 glycerophospholipids, 2 eicosanoids, and 1 saccharolipid (Table S1). Among the 14 differentially regulated carbohydrates, 5 saccharides and glycosides and 2 nucleosides were significantly upregulated in the DSI group, whereas 7 nucleosides were significantly downregulated (Table S1). Only four metabolites were identified in the steroid and steroid derivative category. In the DSI group, one steroid, (6R,10R,13S,17S)-6-hydroxy-10,13-dimethyl-3-oxo-2,3,6,7,8,9,10,11,12,13,14,15,16,17-tetradecahydro-1H-cyclopenta[a]phenanthren-17-yl heptanoate, and one bile acid derivative, 1β-hydroxycholic acid, were significantly increased. In contrast, one steroid, 7α-hydroxy-4-cholesten-3-one, and one vitamin D derivative, doxercalciferol, were significantly downregulated (Table S1).

3.12. Global Metabolic Network Topology Analysis

To investigate the global topological position and functional interactions of differential metabolic pathways from a systems biology perspective, a global metabolic interaction network was constructed by integrating hierarchical information on metabolites, catalytic enzymes, metabolic reactions, and functional pathway modules. Significantly enriched differential pathways were visualized and their topological features characterized. The results revealed 6 core differential pathway modules within the network: fructose and mannose metabolism (sprm00051), beta-alanine metabolism (sprm00410), nucleotide metabolism (sprm01232), purine metabolism (sprm00230), arginine biosynthesis (sprm00220), and pyrimidine metabolism (sprm00240), all of which were significantly differential pathways verified by KEGG enrichment analysis.

Regarding topological distribution and functional connectivity, nucleotide metabolism-related modules (sprm01232, sprm00230, sprm00240) were concentrated in the network's upper functional region. The three modules formed a dense internal network through shared purine/pyrimidine intermediate metabolites, key enzymes, and reaction nodes, constituting a tightly structured, functionally coordinated nucleotide metabolism cluster. This cluster played a core regulatory role in nucleic acid precursor synthesis and nucleotide turnover within the global metabolic network.

Amino acid metabolism-related modules (sprm00220, sprm00410) were located in the network's lower-middle region. The arginine biosynthesis module (sprm00220) was extensively interconnected with several amino acid synthesis and energy metabolism pathways, making it a key hub in the amino acid metabolism network. The beta-alanine metabolism module (sprm00410) sits at the interface between amino acid and nucleotide metabolism, facilitating precursor exchange and metabolic signaling between the two pathway categories.

The fructose and mannose metabolism module (sprm00051) sits in the upstream metabolic region on the left side of the network and connects to multiple downstream synthetic pathways through various hexose intermediate metabolite nodes. It served as a key upstream node for carbon-source supply and energy metabolism, where functional perturbations could broadly affect downstream substance synthesis and energy homeostasis through metabolic cascade effects (Figure 8).

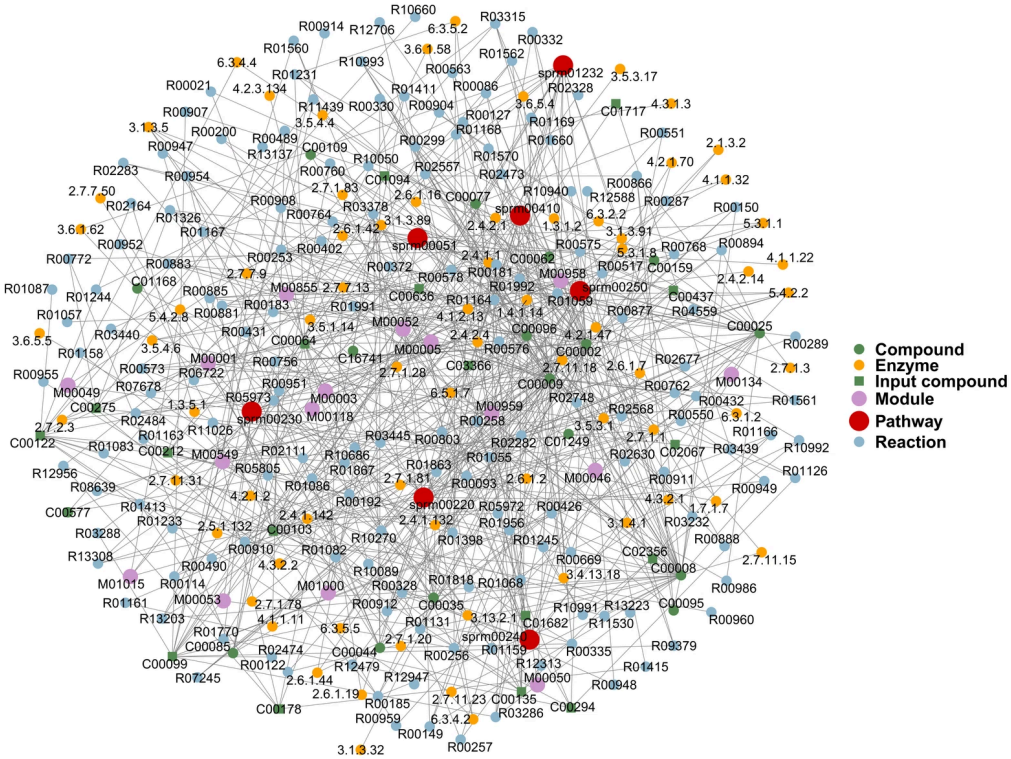


Figure 8. Network analysis for the key hepatopancreatic metabolites and pathways in the comparison between the crab saline group (SAI) and the *CHH* dsRNA treatment group (DSI).

Collectively, the 6 core differential pathways did not exist independently within the global metabolic network. Instead, they formed a synergistically regulated functional network through shared metabolic intermediates and enzyme-catalyzed reaction cascades spanning three key metabolic dimensions, including carbon source metabolism, amino acid synthesis, and nucleotide metabolism. Together, these pathways mediated the metabolic phenotypic remodeling between the two groups. Network topology analysis may support the functional relevance of differential pathways at the systems level, providing a global perspective for subsequent screening of key metabolic targets and mechanistic investigation.

3.13. Correlation Analysis of Differential Metabolite Abundance

Overall, differential metabolites showed a highly modular co-abundance pattern, forming two well-defined, positively correlated metabolite clusters along the diagonal, with extensive significant negative correlations between the two clusters. This pattern may indicate a coordinated, directionally differentiated abundance changes in differential metabolites, rather than independent, random variation.

The first positively correlated module, located in the upper-left region of the heatmap, contained 12 differential metabolites covering diverse structural types: dipeptides (Leu-Thr), amide derivatives, phenol derivatives, medium-chain acylcarnitines (lauroylcarnitine, C12:0), griseophenone B derivatives, quaternary alkaloids (stachydrine), hydroxy-substituted quinoline carboxylic acids, nucleosides (ribothymidine), and amino acid derivatives (homocitrulline). Metabolites within this module showed significant positive correlations ($p < 0.05$), with most correlation coefficients above 0.5 and some exceeding 0.8. This coordinated abundance possibly suggests that metabolites in this module may lie upstream and downstream of the same regulatory pathway or respond in concert to upstream regulatory signals.

The second positively correlated module, located in the lower-right region of the

heatmap, contained 10 differential metabolites, mainly including triazolothiazole derivatives, statine derivatives, hydroxysteroid ketone derivatives, dimethylhistamine, carbohydrate metabolism intermediates (glucose 1-phosphate), biphenylquinoline carboxylic acids, 1β-hydroxycholic acid, lofemizole, dienestrol analogs, and long-chain polyunsaturated dicarboxylic acids. Metabolites in this module also showed extensive, significant positive correlations, probably indicating strong coordination in abundance and forming another functionally linked metabolic regulatory unit (Figure 9).

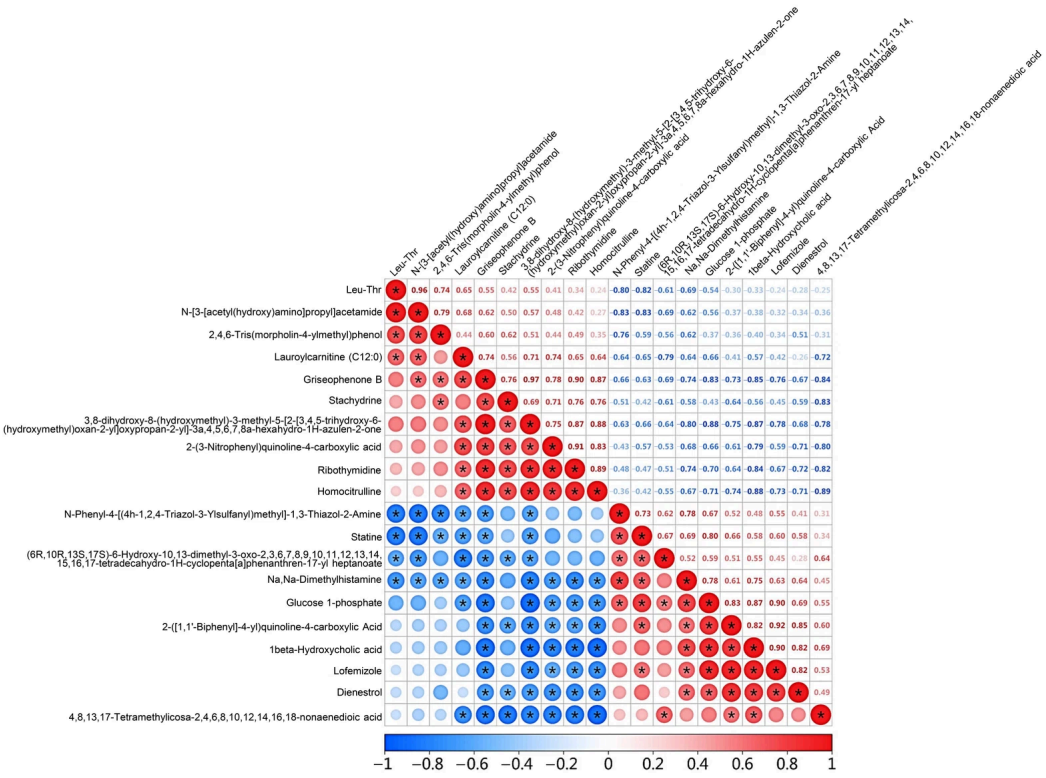


Figure 9. Heatmap of correlation analysis for hepatopancreatic metabolites. *, $p < 0.05$.

The two positively correlated modules also showed extensive significant negative correlations, which may reflect a reciprocal abundance pattern: when metabolite concentrations in the first module increased in one group of samples, those in the second module decreased synchronously. The two coordinated metabolic modules likely correspond to different functional categories, and their reciprocal co-expression pattern constituted a core molecular feature of metabolic phenotypic differences between groups, providing a co-expression-level basis for subsequent key biomarker screening and regulatory mechanism investigation.

4. Discussion

Crustacean hyperglycemic hormone (CHH) is a pleiotropic neuroendocrine factor that involved in carbohydrate homeostasis, energy metabolism, and stress adaptation in crustaceans. The hepatopancreas represents the primary target organ for CHH action, yet the metabolome-wide regulatory landscape of CHH in this tissue remains poorly defined in the mud crab *S. paramamosain*. In this study, RNA interference targeting CHH was applied to female *S. paramamosain* to investigate its regulatory roles in hepatopancreatic function and ovarian development. Injection of *CHH* double-stranded RNA induced appreciable and sustained knockdown of CHH transcription in the eyestalk ganglia. Transcript abundance decreased to approximately 38.11% of the control level at 24 h post-injection and remained below 70% of baseline for at least 5 days. This silencing effi-

cacy falls within the range reported in previous decapod studies targeting CHH-family genes via dsRNA delivery. For instance, silencing efficiencies of 60–80% at 24–72 h post-injection have been documented in *Procambarus clarkii* and *Litopenaeus vannamei*, with suppressive effects lasting 5–10 days depending on dosage and target tissue [20,27]. The durable gene suppression achieved through repeated injections supports this approach for long-term functional studies of CHH during ovarian development.

Histological examination revealed coordinated structural remodeling of the hepatopancreas that paralleled ovarian vitellogenic progression. Over the experimental period, saline-injected control crabs possibly progressed to ovarian stage III [5,8–10], and their hepatopancreatic tubules exhibited increased diameter, luminal dilation, and greater epithelial height compared with stage II individuals at the trial onset. A marked increase in cytoplasmic vacuoles within resorptive cells was also observed, which likely reflects enhanced nutrient mobilization to support yolk deposition. The hepatopancreas is the primary site of exogenous vitellogenin synthesis and nutrient processing in decapod crustaceans, and its histological activation during ovarian maturation has been well documented across species including *Portunus trituberculatus*, *Macrobrachium nipponense*, and *S. paramamosain* [28–30]. In the *CHH*-silenced group, hepatopancreatic tubules showed attenuated luminal dilation and reduced cytoplasmic vacuolization relative to stage-matched controls. These morphological alterations suggest that CHH deficiency may attenuate hepatopancreatic metabolic activity. Such changes may further compromise the capacity of the hepatopancreas to deliver nutrients to the developing ovary. Given the pleiotropic functions of CHH, the hormone may directly act on the hepatopancreas to induce alterations in metabolic-associated physiological and biochemical profiles. CHH deficiency may also perturb other physiological regulatory processes mediated by this peptide, including the biosynthesis of ecdysteroids and methyl farnesoate. Furthermore, prior studies on crustaceans have reported the potential occurrence of CHH receptors within ovarian tissue. Reduced CHH availability may therefore exert additional influences on nutrient uptake and transport dynamics within the ovary. The metabolic crosstalk between the hepatopancreas and ovary remains incompletely characterized to date. Further experimental evidence is required to delineate the precise regulatory mechanisms underlying this interactive process. Similar associations between hepatopancreatic functional status and gonadal growth rate have been reported in studies of hormonal regulation and nutritional challenge [30–32].

To further delineate the molecular basis underlying these histological alterations, untargeted metabolomic profiling was performed on hepatopancreatic samples. A total of 3105 metabolites were identified, with amino acids and derivatives and lipids representing the two dominant superclasses. This metabolite profile is consistent with prior metabolomic surveys of crustacean hepatopancreas, which have consistently identified amino acid and lipid metabolism as core functional modules of the tissue [33–35]. Unsupervised principal component analysis and supervised orthogonal partial least squares discriminant analysis showed clear separation of metabolic profiles between the control and *CHH*-silenced groups, indicative of notable metabolic reprogramming in the hepatopancreas induced by *CHH* deficiency. Across groups, 146 metabolites with significantly altered abundance were identified in this study. Among these candidates, 99 metabolites exhibited markedly reduced levels, while 47 metabolites showed significant increases. This overall trend toward reduced metabolite abundance may reflect broad suppression of biosynthetic and bioenergetic pathways.

Among the differential metabolites, amino acids and derivatives constituted the largest chemical category. The predominance of altered amino acid species aligns with the central roles of the hepatopancreas in protein digestion, amino acid absorption, and

transamination reactions [10,34]. Within this class, the *CHH*-silenced group showed significant depletion of free amino acids, including glutamine, β-alanine, and histidine, whereas methylated amino acids and indole carboxylic acid derivatives were enriched. This shift in the free amino acid pool may reflect both reduced proteolysis and modified amino acid catabolism, a pattern similar to metabolic alterations reported in the hepatopancreas of *L. vannamei* under endocrine disruption [30,34]. Lipid metabolites showed mixed responses: medium- and short-chain acylcarnitines increased, while most fatty acid conjugates and prenol lipids decreased. These lipid alterations may correspond to modified rates of fatty acid oxidation and altered lipid mobilization capacity, processes known to be modulated by eyestalk-derived hormones including CHH [28,36]. Differential abundance was also observed for steroid and bile acid metabolites, consistent with emerging evidence that the crustacean hepatopancreas participates in steroid metabolism and bile acid signaling, with downstream impacts on molting and reproductive physiology [37,38].

At the functional level, the observed metabolic alterations point to multi-pathway regulation of hepatopancreatic metabolism by CHH. Previous work in crayfish has demonstrated that beyond its well-characterized role in carbohydrate homeostasis, *CHH* signaling modulates amino acid and nucleotide metabolism in the hepatopancreas [20,27]. The downregulation of multiple amino acid species in *CHH*-silenced crabs may compromise protein synthetic capacity, including the production of vitellogenin and other yolk precursor proteins in the hepatopancreas [39,40]. Lipid metabolism also appears to be modulated by CHH knockdown, in line with prior evidence linking CHH-family peptides to lipid mobilization and fatty acid trafficking during ovarian maturation. These metabolic shifts may be mediated by downstream effectors such as glucose transporters and metabolic enzymes, a regulatory paradigm described in *Eriocheir sinensis* and other decapod models [23,32].

Metabolite set enrichment analysis, which evaluates coordinated changes across predefined metabolite sets without arbitrary differential abundance thresholds, was applied to identify functionally relevant pathway perturbations. The analysis identified 12 significantly enriched metabolic pathways in the hepatopancreas following *CHH* silencing, equally divided between positive and negative enrichment [41,42]. This bidirectional pattern of pathway perturbation indicates that CHH deficiency drives targeted metabolic reprogramming rather than generalized suppression of hepatopancreatic function. CHH suppression may induce targeted metabolic reprogramming in the hepatopancreas, with selective alterations across distinct functional modules. Carbohydrate and lipid metabolic pathways predominantly exhibit down-regulated trends, pathways related to amino acid and nucleotide metabolism, by comparison, show up-regulated patterns. Silencing of *CHH* in *P. clarkii* has previously been shown to alter pathways spanning carbohydrate, amino acid, and nucleotide metabolism in both muscle and hepatopancreas, and the multi-category enrichment observed here is consistent with those findings [20,27]. Furthermore, the distribution of enriched pathways across diverse functional categories supports a pleiotropic regulatory role for CHH in crustacean hepatopancreas, extending beyond its canonical function in glucose homeostasis [23,33].

Negatively enriched pathways in the DSI group were dominated by glycerophospholipid metabolism, starch and sucrose metabolism, and nucleotide sugar biosynthesis, indicating selective downregulation of specific biosynthetic and energy-metabolism modules. Glycerophospholipid metabolism exhibited the strongest enrichment signal, which may reflect adaptive remodeling of membrane lipid composition and signaling lipid production in response to altered endocrine status. In *S. paramamosain*, hepatopancreatic glycerophospholipid metabolism is tightly coupled to ovarian vitellogenic pro-

gression, as phospholipids are a major constituent of yolk lipids synthesized in the hepatopancreas and transported to the ovary [28,39]. Upregulation of starch and sucrose metabolism and nucleotide sugar biosynthesis further suggests enhanced carbon flux through sugar interconversion pathways, which may compensate for disruptions in primary carbohydrate metabolism caused by *CHH* deficiency [23,43].

Conversely, pathways centered on pyrimidine and purine nucleotide metabolism, along with metabolism of glycine, serine, threonine, and arginine, were positively enriched. The downregulation of nucleotide metabolism aligns with previous findings in crayfish demonstrating that CHH signaling supports nucleotide synthesis and maintains energy charge in peripheral tissues [20,27]. Reduced amino acid biosynthetic capacity may in turn limit substrate availability for protein synthesis, including vitellogenin and other yolk precursor production in the hepatopancreas [39,40]. Collectively, these findings suggest that CHH coordinates hepatopancreatic metabolic activity with ovarian developmental progression in *S. paramamosain*. Combined histological and metabolomic evidence indicates that CHH deficiency suppresses hepatopancreatic digestive and biosynthetic capacity, consistent with the observed delay in vitellogenic development.

Global metabolic network topology analysis revealed that the six core differential pathway modules operate in a coordinated manner and form an interconnected functional network. Nucleotide metabolism-related modules (nucleotide metabolism, purine metabolism, pyrimidine metabolism) clustered in the upper region of the network and formed a tightly coordinated functional cluster via shared intermediate metabolites and enzymatic nodes. This nucleotide metabolism cluster is recognized as a core regulatory unit in crustacean hepatopancreatic metabolic networks, with central roles in nucleic acid precursor supply and cellular energy turnover [30,44]. Amino acid metabolism modules (arginine biosynthesis, β-alanine metabolism) occupied the lower-middle region of the network. Arginine biosynthesis served as a key hub with extensive connections to multiple amino acid synthesis and energy metabolism pathways. The prominent role of arginine metabolism is consistent with its functions in energy storage via phosphoarginine and as a precursor for nitric oxide signaling in crustacean tissues [42,44]. The fructose and mannose metabolism module was positioned as an upstream carbon source node on the left side of the network, linked to multiple downstream synthetic pathways via various hexose intermediates. This topology indicates that perturbations in hexose metabolism can propagate across the entire metabolic network via cascade effects [10,43].

Co-expression correlation analysis further corroborated this modular organization. Two distinct positively correlated metabolite clusters were identified, with extensive significant negative correlations between them. This coordinated abundance pattern may suggest that the two clusters are under opposing regulatory control, and together constitute a core molecular signature of the metabolic shift induced by *CHH* silencing.

Taken together, the metabolomic findings integrate with histological observations to support a model whereby CHH regulates ovarian development, at least in part, by modulating hepatopancreatic metabolic capacity. The reduced hepatopancreatic tubule diameter, diminished epithelial vacuolization, and attenuated secretory activity observed in *CHH*-silenced crabs correspond to the widespread downregulation of nutrient processing and biosynthetic pathways identified at the metabolomic level [29,37].

Several limitations should be noted when interpreting these findings. First, only a single time point during ovarian development was assessed, and the temporal dynamics of CHH-mediated metabolic regulation across the full vitellogenic cycle remain to be characterized. Second, the analysis was restricted to the hepatopancreas, and corresponding metabolic alterations in the ovary and other target tissues remain unexplored.

Third, the molecular mechanisms linking CHH signaling to specific hepatopancreatic metabolic pathways require further investigation via targeted transcriptomic, phosphoproteomic, or metabolomic approaches. Fourth, potential compensatory upregulation of other CHH-family isoforms or related neuropeptides following gene silencing may have attenuated the observed metabolic effects [30,32]. Further studies integrating multi-omic and physiological data are needed to fully elucidate the mechanisms underlying CHH regulation of hepatopancreatic function and reproductive development in portunid crabs.

5. Conclusions

In this study, RNA interference coupled with untargeted metabolomic profiling was employed to systematically characterize the regulatory effects of crustacean hyperglycemic hormone (CHH) on hepatopancreatic metabolism during early ovarian development in *Scylla paramamosain*. CHH deficiency may impose adverse influences on the metabolic activity of the hepatopancreas. CHH knockdown could trigger targeted metabolic reprogramming within this tissue, with selective shifts across distinct functional modules rather than uniform suppression across all metabolic pathways. Pathways associated with carbohydrate and lipid metabolism tended to decline, while several branches of amino acid and nucleotide metabolism exhibited elevated patterns. These observations may suggest that CHH exerts divergent regulatory control over carbon metabolism, lipid turnover, amino acid utilization and nucleotide metabolism in the hepatopancreas. Further work that integrates transcriptomic, proteomic and targeted quantitative assays may help resolve the fine regulatory machinery underlying these metabolic responses.

Supplementary Materials: The following supporting information can be downloaded at https://www.mdpi.com/article/10.3390/biology15232193/s1, Figure S1: Ovarian and hepatopancreatic morphology of *Scylla paramamosain* at the initiation of long-term RNA*i* trial (A) and at the termination in crab saline (SAI, B) and *CHH* dsRNA treatment (DSI, C) groups; Figure S2: The relative CHH gene expression post *GFP* dsRNA injection. Untreated group, without any injection; DSI, *CHH* dsRNA injection group; SAI, crab saline injection group; Figure S3: Glucose level in hemolymph of *S. paramamosain*. Untreated group, without any injection; DSI, *CHH* dsRNA injection group; SAI, crab saline injection group. *, $P < 0.05$, ***, $P < 0.001$; Table S1: Comparison of body weight, GSI, HSI of *Scylla paramamosain* at the initiation of long-term RNAi trial and at the termination in crab saline (SAI) and *CHH* dsRNA treatment (DSI) groups; Table S2: Significantly changed metabolites in hepatopancreas with saline (SAI) and dsRNA (DSI) injection.

Author Contributions: Conceptualization, W.-F.L., Y.C., Z.-Y.Y., and H.H.; methodology, W.-F.L., G.-Y.J., Y.-F.W., S.-Y.Z., and J.S.; software, Y.-F.W., J.S., J.L., X.-Y.X., and Y.-C.Z.; validation, G.-Y.J., Y.-F.W., J.S., J.L., and S.-Y.Z.; formal analysis, G.-Y.J., Y.-F.W., J.L., S.-Y.Z., X.-Y.X., and Y.-C.Z.; investigation, W.-F.L., G.-Y.J., Y.-F.W., A.-Q.Z., S.Z., X.-Y.X., and Y.-C.Z.; resources, W.-F.L., and S.Z.; data curation, W.-F.L., G.-Y.J., J.S., J.L., A.-Q.Z., and X.-Y.X.; writing—original draft, W.-F.L., Y.C., Z.-Y.Y., G.-Y.J., and A.-Q.Z.; writing—review and editing, W.-F.L., Y.C., Z.-Y.Y., and H.H.; visualization, J.S., J.L., A.-Q.Z., S.Z., S.-Y.Z., and Y.-C.Z.; Supervision, W.-F.L., Y.C., Z.-Y.Y., S.Z., and H.H.; Funding acquisition, W.-F.L., Y.C., H.H., and G.-Y.J. All authors have read and agreed to the published version of the manuscript.

Funding: The work was supported financially by the National Natural Science Foundation of China (32661032); the Project of Sanya Yazhou Bay Science and Technology City (grant No. SKJC-JYRC-2024-40); Hainan Provincial Natural Science Foundation of China (grant No. 324MS069); the Scientific Research Foundation of Hainan Tropical Ocean University (No. RHDRC202309); and the Talent Cultivation Fund of Hainan Provincial Academician Innovation Platform.

Institutional Review Board Statement: The animal experiments were fully reviewed and approved by the Laboratory Animal Management and Ethics Committee of Hainan Tropical Ocean University (KJCLL-2026-026).

Data Availability Statement: The original contributions presented in the study are included in the article/Supplementary Material; further inquiries can be directed to the corresponding authors.

Acknowledgments: We are grateful for the help of Shanghai BIOTREE Biological Technology Co., Ltd. (Shanghai, China) in the metabolomics data analysis.

Conflicts of Interest: The authors declare no conflicts of interest.

References

1. Wang, X.; Jin, M.; Cheng, X.; Hu, X.; Zhao, M.; Yuan, Y.; Sun, P.; Jiao, L.; Tocher, D.R.; Zhou, Q. Hepatopancreas transcriptomic and lipidomic analyses reveal the molecular responses of mud crab (*Scylla paramamosain*) to dietary ratio of docosahexaenoic acid to eicosapentaenoic acid. *Aquaculture* **2022**, *551*, 737903. [Google Scholar] [CrossRef]
2. *China Fishery Statistical Yearbook*; China Agriculture Press: Beijing, China, 2026.
3. Liu, G.; Ma, S.; Chen, F.; Gao, W.; Zhang, W.; Mai, K. Effects of dietary lysolecithin on growth performance, feed utilization, intestinal morphology and metabolic responses of channel catfish (*Lctalurus punctatus*). *Aquac. Nutr.* **2019**, *26*, 456–465. [Google Scholar] [CrossRef]
4. Jiang, S.; Qiao, H.; Fu, H.; Gu, Z. Hepatopancreas proteomic analysis reveals key proteins and pathways in regulatory of ovary maturation of *Macrobrachium nipponense*. *Animals* **2023**, *13*, 977. [Google Scholar] [CrossRef] [PubMed]
5. Aaqillah-Amr, M.A.; Hidir, A.; Noordiyana, M.N.; Ikhwanuddin, M. Morphological, biochemical and histological analysis of mud crab ovary and hepatopancreas at different stages of development. *Anim. Reprod. Sci.* **2018**, *195*, 274–283. [Google Scholar] [CrossRef] [PubMed]
6. Waiho, K.; Mustaqim, M.; Fazhan, H.; Norfaizza, W.I.W.; Megat, F.H.; Ikhwanuddin, M. Mating behaviour of the orange mud crab, *Scylla olivacea*: The effect of sex ratio and stocking density on mating success. *Aquacult. Rep.* **2015**, *2*, 50–57. [Google Scholar] [CrossRef]
7. Jiang, X.; Wang, H.; Cheng, Y.; Wu, X. Growth performance, gonad development and nutritional composition of Chinese mitten crab *Eriocheir sinensis* selected for growth and different maturity time. *Aquaculture* **2020**, *523*, 735194. [Google Scholar] [CrossRef]
8. Islam, M.S.; Kader, A.; Paul, P.; Nahar, S. Reproductive Biology of Female Mud Crab, *Scylla Olivacea* Collected from a South-Western Coastal Sub-District, Bangladesh. *Thalassas* **2023**, *39*, 807–816. [Google Scholar] [CrossRef]
9. Tantikitti, C.; Kaonoona, R.; Pongmaneerat, J. Fatty acid profiles and carotenoids accumulation in hepatopancreas and ovary of wild female mud crab (*Scylla paramamosain*, Estampador, 1949). *Songklanakarin J. Sci. Technol.* **2015**, *37*, 609–616. [Google Scholar]
10. Wu, Q.; Waiho, K.; Huang, Z.; Li, S.; Zheng, H.; Zhang, Y.; Mhd Ikhwanuddin, M.; Lin, F.; Ma, H. Growth performance and biochemical composition dynamics of ovary, hepatopancreas and muscle tissues at different ovarian maturation stages of female mud crab, *Scylla paramamosain*. *Aquaculture* **2020**, *515*, 734560. [Google Scholar] [CrossRef]
11. Duangprom, S.; Saetan, J.; Phanaksri, T.; Songkoomkrong, S.; Surinlert, P.; Tamtin, M.; Sobhon, P.; Kornthong, N. Acceleration of ovarian maturation in the female mud crab with RNA interference of the vitellogenesis-inhibiting hormone (VIH). *Front. Mar. Sci.* **2022**, *9*, 880235. [Google Scholar] [CrossRef]
12. Zhang, Y.; Jiang, S.; Qiao, H.; Xiong, Y.; Fu, H.; Zhang, W.; Gong, Y.; Jin, S.; Wu, Y. Transcriptome analysis of five ovarian stages reveals gonad matration in female *Macrobrachium nipponense*. *BMC Genom.* **2021**, *22*, 510. [Google Scholar] [CrossRef] [PubMed]
13. Quackenbush, L.S. Yolk Synthesis in the Marine Shrimp, *Penaeus vannamei*. *Am. Zool.* **2015**, *41*, 458–464. [Google Scholar]
14. Subramoniam, T. Mechanisms and control of vitellogenesis in crustaceans. *Fish. Sci.* **2011**, *77*, 1–21. [Google Scholar] [CrossRef]
15. Rani, K.; Subramoniam, T. Vitellogenesis in the mud crab *Scylla serrata* in vivo isotope study. *J. Crust. Biol.* **1997**, *17*, 659–665. [Google Scholar] [CrossRef]
16. Santos, E.A.; Nery, L.E.M.; Keller, R.; Goncalves, A.A. Evidence for the involvement of the crustacean hyperglycemic hormone in the regulation of lipid metabolism. *Physiol. Zool.* **1997**, *70*, 415–420. [Google Scholar] [CrossRef] [PubMed]
17. Webster, S.G.; Keller, R.; Dircksen, H. The CHH-superfamily of multifunctional peptide hormones controlling crustacean metabolism, osmoregulation, moulting, and reproduction. *Gen. Comp. Endocrinol.* **2012**, *175*, 217–233. [Google Scholar] [CrossRef]

[PubMed]

18. Lee, C.Y.; Tsai, K.T.; Tsai, W.S.; Jiang, J.Y.; Chen, Y.J. Crustacean Hyperglycemic Hormone: Structural Variants, Physiological Function, and Cellular Mechanism of Action. *J. Mar. Sci. Technol.-Taiw.* **2014**, *22*, 9. [Google Scholar]
19. Chen, H.Y.; Toullec, J.Y.; Lee, C.Y. The crustacean hyperglycemic hormone superfamily: Progress made in the past decade. *Front. Endocrinol.* **2020**, *11*, 578958. [Google Scholar] [CrossRef] [PubMed]
20. Li, W.; Chiu, K.H.; Tien, Y.C.; Tsai, S.F.; Shih, L.J.; Lee, C.H.; Toullec, J.Y.; Lee, C.Y. Differential effects of silencing crustacean hyperglycemic hormone gene expression on the metabolic profiles of the muscle and hepatopancreas in the crayfish Procambarus clarkii. *PLoS ONE* **2017**, *12*, e0172557. [Google Scholar] [CrossRef] [PubMed]
21. Fu, C.; Huang, X.; Gong, J.; Chen, X.; Huang, H.; Ye, H. Crustacean hyperglycaemic hormone gene from the mud crab, *Scylla paramamosain*: Cloning, distribution and expression profiles during the moulting cycle and ovarian development. *Aquacult. Res.* **2016**, *47*, 2183–2194. [Google Scholar] [CrossRef]
22. Sun, D.; Lv, J.; Gao, B.; Liu, P.; Li, J. Crustacean hyperglycemic hormone of *Portunus trituberculatus*: Evidence of alternative splicing and potential roles in osmoregulation. *Cell Stress Chaperones* **2019**, *24*, 517–525. [Google Scholar] [CrossRef] [PubMed]
23. Liu, A.; Liu, J.; Chen, X.; Lu, B.; Zeng, C.; Ye, H. A novel crustacean hyperglycemic hormone (CHH) from the mud crab *Scylla paramamosain* regulating carbohydrate metabolism. *Comp. Biochem. Phys. A* **2019**, *231*, 49–55. [Google Scholar] [CrossRef] [PubMed]
24. Li, W.F.; Li, S.; Lin, Z.Y.; Peng, H.; Wang, K.J. Hepatopancreas and ovary transcriptome analyses reveal key physiological changes in the pubertal molt of mud crabs *Scylla paramamosain*. *Comp. Biochem. Physiol. D.* **2026**, *61*, 102026. [Google Scholar] [CrossRef] [PubMed]
25. Li, W.F.; Li, S.; Liu, J.; Wang, X.F.; Chen, H.Y.; Hao, H.; Wang, K.J. Vital Carbohydrate and Lipid Metabolites in Serum Involved in Energy Metabolism during Pubertal Molt of Mud Crab (*Scylla paramamosain*). *Metabolites* **2021**, *11*, 651. [Google Scholar] [CrossRef] [PubMed]
26. Li, S.; Li, W.; Chen, F.; Zhu, X.; Chen, H.Y.; Hao, H.; Wang, K.J. Metabolomic and transcriptomic analysis reveals immune and hormone modulation at the molting stage of juvenile mud crabs challenged with *Staphylococcus aureus* and *Vibrio alginolyticus*. *Aquaculture* **2023**, *575*, 739775. [Google Scholar] [CrossRef]
27. Li, W.; Chiu, K.H.; Lee, C.Y. Regulation of amino acid and nucleotide metabolism by crustacean hyperglycemic hormone in the muscle and hepatopancreas of the crayfish *Procambarus clarkia*. *PLoS ONE* **2019**, *4*, e0221745. [Google Scholar]
28. Fu, Y.; Zhang, F.; Ma, C.; Wang, W.; Liu, Z.; Chen, W.; Zhao, M.; Ma, L. Comparative metabolomics and lipidomics of four juvenoids application to *Scylla paramamosain* hepatopancreas: Implications of lipid metabolism during ovarian maturation. *Front. Endocrinol.* **2022**, *13*, 886351. [Google Scholar] [CrossRef] [PubMed]
29. Li, N.; Zhou, J.; He, C.; Fu, Y.; Wang, C.; Liu, L.; Meng, K.; Li, Y.; Zhu, Z.; Huang, L.; et al. GC-MS-based metabolomics reveal that light intensity during indoor overwintering affects the metabolism of *Scylla paramamosain*. *Aquac. Res.* **2021**, *52*, 1013–1025. [Google Scholar] [CrossRef]
30. Ren, Y.; Wang, W.; Liu, Z.; Luo, M.; Fu, Y.; Zhang, F.; Ma, C.; Zhao, M.; Chen, W.; Jiang, K.; et al. Insight of vitellogenesis patterns: A comparative analysis of the differences between the primary and secondary vitellogenesis period in the ovary, hepatopancreas, and muscle of mud crab, *Scylla paramamosain*. *Front. Genet.* **2022**, *13*, 965070. [Google Scholar] [CrossRef] [PubMed]
31. Zeng, X.; Huang, C.; Deng, Z.; Xiao, Y.; Zou, P.; Wang, Y. Lipid metabolism in hepatopancreas and ovaries of the mud crab *Scylla paramamosain* during vitellogenesis. *Comp. Biochem. Physiol. D.* **2026**, *60*, 101891. [Google Scholar] [CrossRef] [PubMed]
32. Zhang, L.; Sun, L.; Song, G.; Wang, B.; Cui, Y.; Liu, F.; Li, Y.; Wang, Z. Genome-Wide Identification and Expression of Neuropeptides and Their Expression Patterns After RNAi of CHH Genes in Pacific White Shrimp *Litopenaeus vannamei*. *Biology* **2024**, *13*, 1038. [Google Scholar] [CrossRef] [PubMed]
33. Zhang, X.; Pan, L.; Tong, R.; Li, Y.; Si, L.; Chen, Y.; Wu, M.; Wang, Q. Effects of crustacean hyperglycaemic hormone RNA interference on regulation of glucose metabolism in *Litopenaeus vannamei* after ammonia-nitrogen exposure. *Br. J. Nutr.* **2022**, *127*, 823–836. [Google Scholar] [CrossRef] [PubMed]
34. Sun, S.; Guo, Z.; Fu, H.; Ge, X.; Zhu, J.; Gu, Z. Based on the metabolomic approach the energy metabolism responses of oriental river prawn *Macrobrachium nipponense* hepatopancreas to acute hypoxia and reoxygenation. *Front. Physiol.* **2018**, *9*, 76. [Google Scholar] [CrossRef] [PubMed]
35. Li, D.; Mao, B.; Wang, Y.F. Metabolome analysis on hepatopancreas of *Procambarus clarkii* with different stress resistances. *Acta Hydrobiol. Sin.* **2023**, *47*, 1211–1219. [Google Scholar]

36. Sun, Y.; Zhang, Y.; Liu, Y.; Xue, S.; Geng, X.; Hao, T.; Sun, J. Changes in the Organics Metabolism in the hepatopancreas induced by eyestalk ablation of the chinese mitten crab *Eriocheir sinensis* determined via transcriptome and DGE analysis. *PLoS ONE* **2014**, *9*, e95827. [Google Scholar] [CrossRef] [PubMed]
37. Xie, S.; Deng, Y.; Tang, Z.; Zhan, W.; Peng, H.; Xu, T.; Tian, Y.; Bao, Y.; Xu, J.; Zhu, T.; et al. Bile acid metabolites enhance molting response and improve energy metabolism in *Scylla paramamosain* via cooperative regulation of cerebral ganglia and hepatopancreas. *ACS Nutr. Sci.* **2026**, *1*, 48–68. [Google Scholar] [CrossRef]
38. Wang, W.; Wu, X.; Liu, Z.; Zheng, H.; Cheng, Y. Insights into hepatopancreatic functions for nutrition metabolism and ovarian development in the crab *Portunus trituberculatus*: Gene discovery in the comparative transcriptome of different hepatopancreas stages. *PLoS ONE* **2014**, *9*, e84921. [Google Scholar] [CrossRef] [PubMed]
39. Puengyam, P.; Tsukimura, B.; Utarabhand, P. Molecular characterization of hepatopancreas vitellogenin and its expression during the ovarian development by in situ hybridization in the banana shrimp *Fenneropenaeus merguiensis*. *J. Crustac. Biol.* **2013**, *33*, 265–274. [Google Scholar] [CrossRef]
40. Li, Z.; Zhou, M.; Ruan, Y.; Chen, X.; Ren, C.; Yang, H.; Zhang, X.; Liu, J.; Li, H.; Zhang, L.; et al. Transcriptomic analysis reveals yolk accumulation mechanism from the hepatopancreas to ovary in the pacific white shrimp *Litopenaeus vannamei*. *Front. Mar. Sci.* **2022**, *9*, 948105. [Google Scholar] [CrossRef]
41. Subramanian, A.; Tamayo, P.; Mootha, V.K.; Mukherjee, S.; Ebert, B.L.; Gillette, M.A.; Paulovich, A.; Pomeroy, S.T.; Golub, T.R.; Lander, E.S.; et al. Gene set enrichment analysis: A knowledge-based approach for interpreting genome-wide expression profiles. *Proc. Natl. Acad. Sci. USA* **2005**, *102*, 15545–15550. [Google Scholar] [CrossRef] [PubMed]
42. Pang, Z.; Lu, Y.; Zhou, G.; Hui, F.; Xu, L.; Viau, C.; Spigelman, A.; MacDonald, P.; Wishart, D.; Li, S.; et al. MetaboAnalyst 6.0: Towards a unified platform for metabolomics data processing, analysis and interpretation. *Nucleic. Acids Res.* **2024**, *52*, 398–406. [Google Scholar] [CrossRef] [PubMed]
43. Li, N.; Zhou, J.; Wang, H.; Mu, C.; Shi, C.; Liu, L.; Wang, C. Transcriptome analysis of genes and pathways associated with metabolism in *Scylla paramamosain* under different light intensities during indoor overwintering. *BMC Genom.* **2020**, *21*, 775. [Google Scholar] [CrossRef] [PubMed]
44. Duan, Y.; Xiao, M.; Wang, Y.; Huang, J.; Yang, Y.; Li, H. The high temperature stress responses in the hepatopancreas of *Litopenaeus vannamei*: From immune dysfunction to metabolic remodeling cascade. *Front. Immunol.* **2025**, *16*, 1631655. [Google Scholar] [CrossRef] [PubMed]

Disclaimer/Publisher's Note: The statements, opinions and data contained in all publications are solely those of the individual author(s) and contributor(s) and not of MDPI and/or the editor(s). MDPI and/or the editor(s) disclaim responsibility for any injury to people or property resulting from any ideas, methods, instructions or products referred to in the content.